UiT
THE ARCTIC
UNIVERSITY
OF NORWAY

Faculty of Science and Technology
Department of Physics and Technology

Comparison of the Ice Watch Database and Sea Ice Classification from Sentinel-1 Imagery

Joakim Lillehaug Pedersen

FYS-3941 Master's thesis in applied physics and mathematics 30 SP

December - 2019

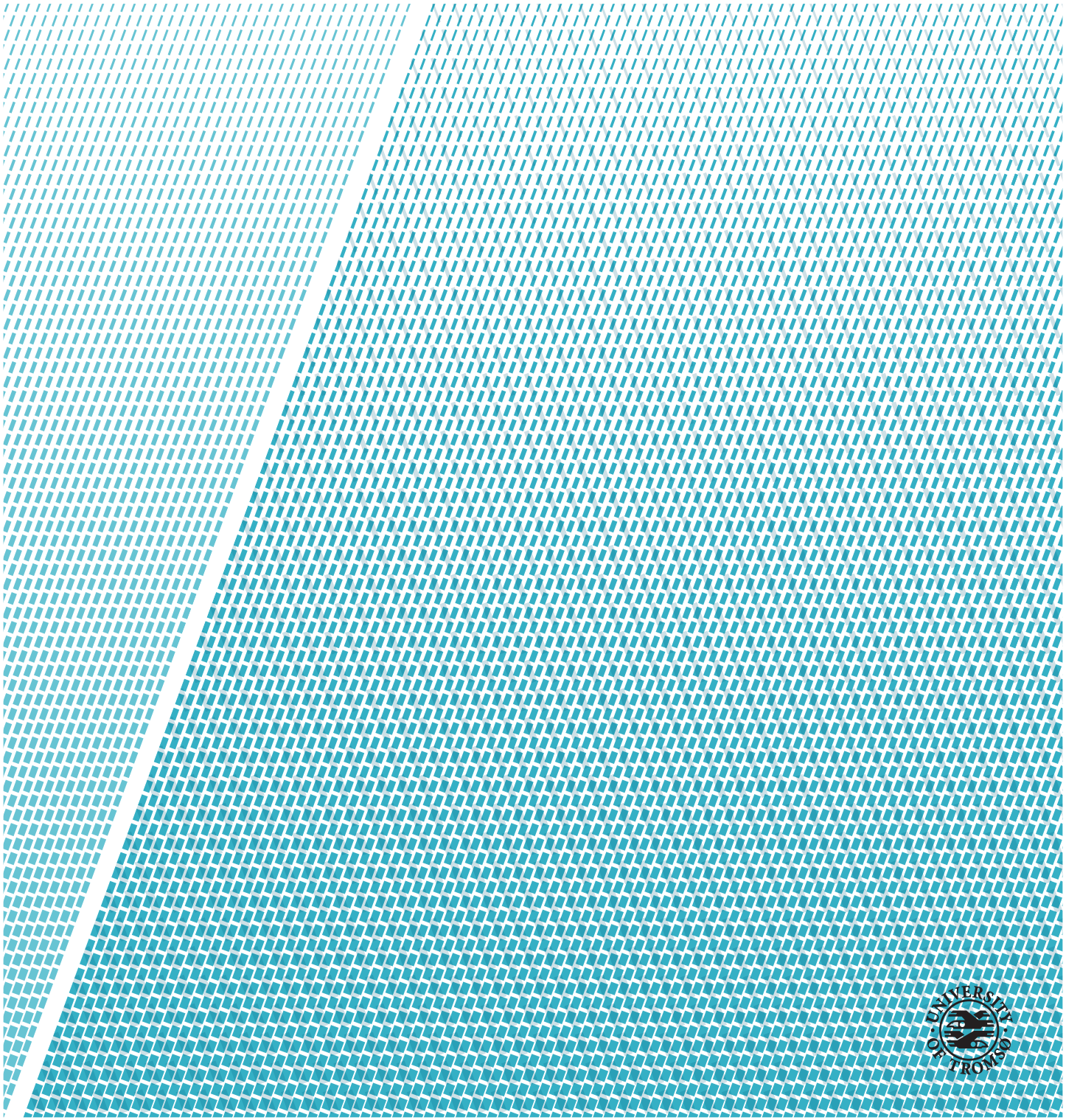

Abstract

In this thesis, we investigate the potential use of in-situ sea ice observations from the Ice Watch database as ground truth data for an automated classification algorithm of sea ice types from Sentinel-1 SAR data. The Ice Watch database and the Sentinel-1 data archive are searched for in-situ observations and satellite data acquisitions in Extra Wide swath mode overlapping in both space and time. Time differences of up to a maximum of 12 hours are accepted and included in this investigation. The Sentinel-1 data is downloaded in Ground-Range Detected format at medium resolution and thermal noise correction, radiometric calibration and additional multilooking with a 3-by-3 window is applied. Different ice types in the images are then classified with the Gaussian IA classifier developed at UiT. The resulting image with ice type labels is geo-located and aligned with the in-situ observation from the Ice Watch database. A grid of 25-by-25 pixels around the location of the Ice Watch observation is extracted. For data points with a large time difference between in-situ observation and satellite data acquisition, a sea ice drift algorithm is applied to estimate and correct for possible influence of ice drift between the two acquisition times. Correlation and linear regression is investigated between a total number of 123 observation and the classified area around the observation. In addition, per class accuracy for the trained ice types in the classifier is investigated. A medium to strong positive correlation is found between types of ice and a weakly negative to no correlation was found for sea ice concentration. "Second-/Multiyear ice" separation achieves the highest score with 93.8 % per class accuracy. The second highest scoring class is "Deformed First-Year Ice", for which 48.1 % per class accuracy is achieved. The thinner ice performs poorly due to the low number of representative of observations from these classes. Based on the findings there is a relationship between the reported observations from the Ice Watch database and the classified Sentinel-1 images. The ability to separate the older and deformed ice types from younger level ice is present.

Acknowledgements

First I would like to thank my supervisors Ass. Prof. Anthony Doulgeris, Nick Hughes and Penelope Mae Wagner for guidance and supervision during the master's degree work. Secondly, I want to thank Johannes Lohse for helping with concepts, technical details and for being available during the master thesis period. Many questions were asked and answered.

Thanks to co-workers at The Norwegian Meteorological Institute for giving advice regarding map projection and QGIS.

To my fellow students, thanks for working besides me during these years. And to those who have proofread, thank you!

I am grateful to my mother, my father, and my four sisters for supporting me through the last five years of study. Without all of you, this journey would have been gray and cumbersome.

Finally I want to thank Liv and Ennea, for being a part of my life and brining joy to each day.

Joakim Lillehaug Pedersen
Tromsø, December 2019

Acronyms

ANN Artificial Neural Network

ASPEcTS Antarctic Sea Ice Processes & Climate

CIRFA Centre for Integrated Remote Sensing and Forecasting for Arctic Operations

CIS Canadian Ice Service

EO Earth Observation

EW Extra Wide swath mode

GRDM Ground-Range Detected format at Medium Resolution

GT Ground Truth

IA Incident Angle

IWD Ice Watch Database

MET The Norwegian Meteorological Institute

RS Remote Sensing

S-1 Sentinel-1

SAR Synthetic-Aperture Radar

SNAP Sentinel Application Platform

SVM Support Vector Machine

UiT University of Tromsø - The Arctic University of Norway

Contents

List of Figures

List of Tables

1 Introduction

1.1 Motivation

Global monitoring of earth has been an important scientific field in many branches for the reason of keeping track of climate, meteorology, marine traffic, environmental and more[36; 19; 9; 10]. Remote Sensing (RS) from space with optical or radar sensors is by far the best method to continuously monitor large area of the Earth surface.

To get a fully automated classification scheme that is able to separate and classify different types types of ice without human interaction has been of interest for many countries and organization for years, e.g. The Norwegian Meteorological Institute (MET) and Canadian Ice Service (CIS). Researchers and scientist can use SAR data from polar areas as an indicator in the global climate monitoring[42]. At this point in time, there exist no such algorithm with sufficient accuracy for operational use.

Classification of sea ice types from SAR data is difficult for many reasons. The radar signal is influenced by both the radar parameters and the surface parameters. Radar parameters include frequency, polarization and local incidence angle. The general surface parameters are the surface roughness and the dielectric properties of the surface. In the case of sea ice, the problem is additionally complicated by seasonal variation causing the ice to change characteristic, difference in the salinity in water due to geographical location, mixed ice types, and error due to the incident angle of satellite sensor. All these

factors influences the image.

Another challenge is the lack of training and validation data for a supervised machine learning algorithm. These algorithms need an abundance of in-situ observation called Ground Truth (GT). At the moment there are few such observations of ice types since this requires that skilled analyst is at the actual location of interest to measure the ice type. Collecting measurement is difficult, time consuming and economically expensive in a vast area like the Arctic. Few expeditions do this on a yearly basis.

1.2 Previous work in the field of supervised classification of sea ice

To automatize the process of classifying SAR-images a variety of supervised algorithms have been tested. There exist numerous studies with many combinations of classifiers and different input features to these classifiers, as well as a variety of sources for ground truth to train and validate the result.

Many investigation have been done to separate ice and water by the use of (semi)automatic algorithm with SAR data[38; 20; 13; 17; 16].

Two popular machine learning algorithms that have been extensively used is Artificial Neural Network (ANN)[34; 37; 4; 21; 45] and Support Vector Machine (SVM)[43; 23; 18; 25]. These methods require prior knowledge of the underlying data, but with no information about statistical content. Other methods often used are Bayesian classification[45; 39] and Maximum likelihood[30; 15]. These two latter mentioned method are based on prior statistical knowledge of the distribution of classes.

Many papers does an extended feature analysis to separate good quality features from the redundant ones. In [37] they investigate 18 polarimetric features while in [43; 4; 23; 45; 39] they used texture feature, often in addition to backscatter intensity which can be extracted from the grey level co-occurrence matrix as done in [39; 34; 23; 39; 25]. Atmospheric parameters and Multisensor Analyzed Sea Ice Extent [18] has also been tested as input to a machine learning algorithm.

Often has manually drawn ice charts been used as ground truth[43; 21; 45; 18], but have often been seen as a source that is subject to human interpretation and therefore biased. In addition the lower resolution in drawn ice charts is a disadvantage when compared to Synthetic-Aperture Radar (SAR) sensors.

Two reoccurring issues in many studies are the classification error of Extra Wide swath mode (EW) images due to the incident angle effect[30; 37], and the dynamic noise-floor pattern in Sentinel-1 (S-1) images due to aligning different acquisition strips together. These problems are described in detail in [11]

This is only a small portion of investigations conducted since the space born SAR became a primary source of global monitoring of ice. A more extensive and detailed overview of previous work in the field of classification of sea ice can be further studied in article [44]

1.3 Objective

In this thesis the focus will be on sea ice monitoring with the use of SAR. More specific: ice type classification in a supervised manner by the use of the Ice Watch Database (IWD), and imagery acquired from S-1 in EW.

I will compare observations from this database with classified, near-time coincident S-1 imagery, and investigate if the database can potentially be used as ground truth for a classification algorithm. A conclusion regarding the usefulness of comparing this database with S-1 images will be presented.

The classifier used will be the "Gaussian IA Classifier" [26] developed at University of Tromsø - The Arctic University of Norway (UiT).

1.4 Overview of chapters/short description

Chapter 2 gives an overview of the theory needed to follow the investigations conducted in this thesis. It starts with basic explanation of machine learning, supervised learning and the importance of training data collection. Here, IWD will also be discussed: what it is, why it potentially is a good source for training data and how can observation be collected. A general introduction to SAR and S-1 are given before the explanation of the preprocessing stages of satellite images and the challenge with "The incident angle effect" in EW mode is stated. Well known techniques used and the chosen machine learning scheme, "The Gaussian IA-classifier", is also explained.

Chapter 3 goes through, in detail, how the IWD and S-1 imagery were prepared, aligned and compared. Choices regarding parameters from IWD, criteria for S-1 images and how the viewing distance and ice drift are dealt with.

Chapter 4 yields the results from the investigation. From section 4.2 through section 4.4 we follow the results from a single image pair. This for visual impression and explanation of how the investigation for all image pairs are conducted. Section 4.5 and 4.6 shows the general results when comparing IWD with S-1 images. The remaining chapter is for discussion.

Chapter 5 summarizes the conclusions and an outlook for possible future work is presented.

2

Theoretical background

2.1 Why Arctic?

The Arctic environment plays an important role in global weather and climate systems. Energy in the atmosphere contributes to the weather systems and how they are created[6]. The Arctic spans a huge area and sea ice acts as reflector for radiation from space. When sea ice melts the reflection from sea ice is changed to energy absorption in water. This decrease in albedo in water versus ice leads to an increase in global temperature.

Less ice in Arctic areas has turned the eyes of the industry to look north. Increased marine traffic and offshore operation amplifies the need for good and reliable information about the ice condition for safe navigation and operation in the area.

RS data is the best method to continuously monitor a vast area such as the Arctic. In particular, SAR data is a preferred tool, because of its large spatial coverage at relatively high resolution, and its all-day and all-weather capability (see section 2.3.2)

2.2 Supervised learning and training data collection

In the machine learning world there are mainly two ways of solving a problem: supervised and unsupervised. Both aims to recognize patterns in the dataset of interest to segment them into subsets, popularly called classes. In addition, it exists a hybrid branch between these two, namely called semisupervised.

If we have prior knowledge about the classes and training data (in our case GT data), the task can be solved in a supervised fashion. GT can be observation at the area of interest or other good quality measurement that can give us prior knowledge and the "answer" for the challenge we wish to solve. In the other way of solving a problem, namely the unsupervised, trained data is not available. The latter technique can only group instances of similar attributes into groups and have to be further investigated to give a physical meaning.

One of the great challenges in supervised classification of ice is the lack of training data, which a supervised approach requires abundance of. For a Earth Observation (EO) classification task this means that experts needs to be on ground gathering in-situ observation which can be fed to the classifier. It does not come as a surprise that for a vast remote area like Arctic this is a time consuming and expensive affair. Few ships make trips to the Arctic on a yearly basis. Even fewer have experts able to distinguish the many types of ice existing to a satisfactory level. These factors in combination makes good quality ice observation rare.

The Ice watch database is a database consisting of good quality ice observation from experts and will therefore be investigated if it can be used as GT for classification of S-1 images.

2.3 Two sources of information

2.3.1 Ice Watch database

From a scientific point of view, it is important to have a consistent framework of gathering data within a field of study. To maintain good quality observations across seasons, geographic location and different observers, we need a standardized way of gathering and processing the information retrieved from the expedition of interest. The ice watch database is no different, and when observations is collected for this purpose, [2] must be followed.

[2] was published by the University of Alaska Fairbanks and has the intention to standardise sea ice observations from ships with a protocol of how to conduct such observations, and a software tool for entering and archiving data, called ”ASSIST”.

Ice Watch Assist was modeled after Antarctic Sea Ice Processes & Climate (ASPEcTS) where the aim of this model was to understand the role of Antarctic sea ice.

From November 2019, the database was transferred to, and is managed by, MET who also recently has received funding from the European Space Agency to develop this project further. IWD can now be accessed from their web site [3].

Collection of sea ice observation

The backbone of sea ice characterization is the egg code, which is e.g. used in ice type charts generated by the CIS. The ice in a region is classified in three different categories based on the type of ice. From thickest to thinnest we have Primary, Secondary and Tertiary ice types. A not so common practice is to report additional, minor ice classes. For the three main types, the concentration, stage of development, and the form of ice are reported. The ice watch manual is built with the egg code in mind.

According to the manual, the observers should conduct their observation on the bridge or on one of the ships upper decks. The optimal location is where the observer have a 360 degree view. The ice is viewed with a radius of approximately one nautical mile from the ship.

A watch can consist of several observers to cross compare their interpretation of the site for the purpose of consistency. The standard procedure is to make an observation every hour, on the hour, when the ship is making speed through water. Observation should not be conducted when the ship has not moved within the ice pack. It is recommended that it has moved at least three nautical miles during a ten minute period between observations. This is to ensure that the same ice is not recored several times.

For each observation the observer can fill in up to 113 parameters divided in five different categories: General, Ice, Meteorology, Photos, and Comments. However only five of these 113 parameters are mandatory:

- Primary observer

- Observation date and time
- Latitude and longditude
- Total ice concentration
- Visibility

For a detailed description of all the parameters see [2].

2.3.2 Satelitte images

Synthetic aperture radar

This section about SAR is based on a review of chapter 7 in [7] and chapter 5 in [12].

There are mainly two types of sensors onboard a satellite: Active and passive sensors. Active sensors transmits and receives their own signal while passive sensors only receives energy emitted from the Earth's surface. Synthetic aperture radar is an active sensor, meaning transmitting its own electromagnetic waves while receiving the backscattered fraction of echo from the illuminated surface. There are many advantages with active sensors over passive sensors. Since the sensor actively generates and transmits its own signal, the properties of the signal are known in detail. Furthermore, no natural light source (sun) is needed and data can be acquired independently of sunlight conditions. By comparing transmitted energy with the received energy, active sensors are capable of a precise interpretation of the surface.

One of the big advantages with SAR is the synthesizing of a long antenna. All the period an object is illuminated by the transmitted wave, the complete history of the reflection, from this object, is stored. Later reconstruction of this history gives the same results as if it was received by one large antenna with the size equal the distance travelled by the satellite. When an objects is "in front" of a moving satellite it reflects an increased frequency from the transmitted wave, compared to when it is "behind" the same satellite. This is known as the 'Doppler effect'. Prior information of the frequency shift, enables the system to correctly position objects and to synthesize a large antenna, even though the physical antenna is much shorter.

The wavelength of the electromagnetic wave in the microwave region is from 1 mm to 1 m and is therefore larger than particles in the atmosphere. As stated in [12], "The advantage of the microwave imaging radiometer, relative to visible

or near-infrared imager, is the fact that it acquires data all the time, even during the long dark winter season during time of haze or cloud cover" (p. 172). The atmosphere is almost completely transparent at microwave wavelengths and data acquisition is thus not affected by cloud or weather conditions.

By measuring different properties of the backscattered energy, such as intensity, polarization and phase, an image of the illuminated area can be interpreted and formed.

Polarization

An electromagnetic wave is composed of both electric and magnetic field oriented perpendicular to each other. The polarization of a radar signal reveals the orientation of the electromagnetic energy transmitted and received by an antenna. A sensor that sends and receives horizontally(or vertically) oriented electromagnetic waves is called single polarized. If a sensor can receive horizontally and vertically oriented waves it is called dual polarized. For single polarized, the received signal is in the same polarization, yielding channel HH or VV. Dual polarization transmits in H or V and receives in both polarization, yielding channel HH/HV and VV/VH. If a satellite has quad polarization configuration it transmits and receives on both polarization yielding the channels HH/HV/VH/VV. Different surface properties may yield the same backscatter in one channel, but different in others. When doing analysis, expert knowledge and experience of the backscatter response in the different channels are vital.

SAR and sea ice

The received echo from the transmitted wave is dependent on many factors: polarization, incident angle, radar frequency and the retrieved backscatter intensity from illuminated surface. These again are dependent of the surface physical and dielectric properties[44; 10]. Ice thickness can not be seen directly with the use of SAR and the stage of development is difficult to separate due to the ambiguity in backscatter from ice[32]. Also backscatter from windy waters can overlap with several ice types[28]. In addition, different locations and seasons changes the characteristics of the ice surface and the signal-ice interference due to differences in salinity and melting/freezing seasons[33; 6], thereby making the separation of different types of ice, by the use of spacecrafts, challenging.

Sentinel-1

The use of SAR is an invaluable tool, and often the only source in monitoring the Arctic environment. The need for covering such a huge area daily, sets requirement to the sensor in use.

According to [1; 14] the S-1 mission consist of two near-polar, sun-synchronous orbit C-band(microwave) SAR-sensors, operating day and night. Capable of capturing images regardless of weather, these SAR-sensors deliver images in four different modes, resolution down to 1.7x4.3 m for level-1 products and coverage up to 400 km. The sensors have dual polarisation capability and a short revisiting time. The mission is currently composed of two satellites: Sentinel-1A and Sentinel-1B. Sharing the same orbital plane, but 180 degrees phased making SAR-interferometry possible.

S-1 produces a consistent long term data archive built for application based on long time series, making it a reliable source for EO data and monitoring of the Arctic environment.

Images from this sensor can be freely accessed and downloaded via the "Copernicus sentinel open access hub"[1] and is the source for EO data used in this thesis.

Preprocessing

Thermal noise removal
Thermal noise comes from properties of the sensor. Characteristic of the sensor itself causes the measured signal in each imaging swath to focus around the middle of the swath. For a multi-swath acquisition mode, like EW, this noise has different intensity in each sub-swath. An effect of this is a sub-swath variation from the middle of the swath to the outer boundaries[35]. This artifact in the image can be reduced. Since this artifact comes from properties of the sensor it is known and can be accounted for. For each product a denoising vector can be applied to correct for thermal noise.

Radiometric calibration:
The raw data captured by the sensor is stored as digital numbers in the form of integers values. These values need to be converted to physical units do get a relationship to other images or to features on the ground. The radiometric calibration corrects for the geometric viewing conditions, date dependency and the distance from the sensor to the illuminated surface. It converts the digital

1. https://scihub.copernicus.eu/dhus/#/home

numbers into radar cross-section[5]. This makes comparison from different sensors, taken at different points in time, possible.

Multilooking
The process of multilooking reduces speckle noise(salt-and-pepper noise from constructive or destructive interference between electromagnetic waves) and thermal sensor noise. This is done either in the spatial domain or Fourier domain. In spatial domain it is done by the use of an average running filter over a neighborhood of adjacent pixels. By transforming the image to Fourier domain the same can be achieved by splitting the image in the wanted number of looks and then averaging over them. An effect by multilooking is a degradation of the resolution in the sense that values in adjacent pixels are being mixed.

In this work we use S-1 data in EW mode in Ground-Range Detected format at Medium Resolution (GRDM). This product has a pixel spacing of 40-by-40 m at an actual resolution of 93-by-87m. After multilooking the resolution is closer to 120-by-120 m.

The incident angle effect in EW-swath mode

A side-looking sensor yields different incident angle on areas on the ground within an image. The effect of this is a decay in intensity backscatter from near-range to far-range across the image. This makes both human and statistical interpretation a challenging task. Visually the image is brighter closer to the satellites position than further away and the problem is increasing with a greater incident angle range as in a satellite image acquired in EW mode. This artifact is popular called ”The incident angle effect” and is visualized in Figure 2.1

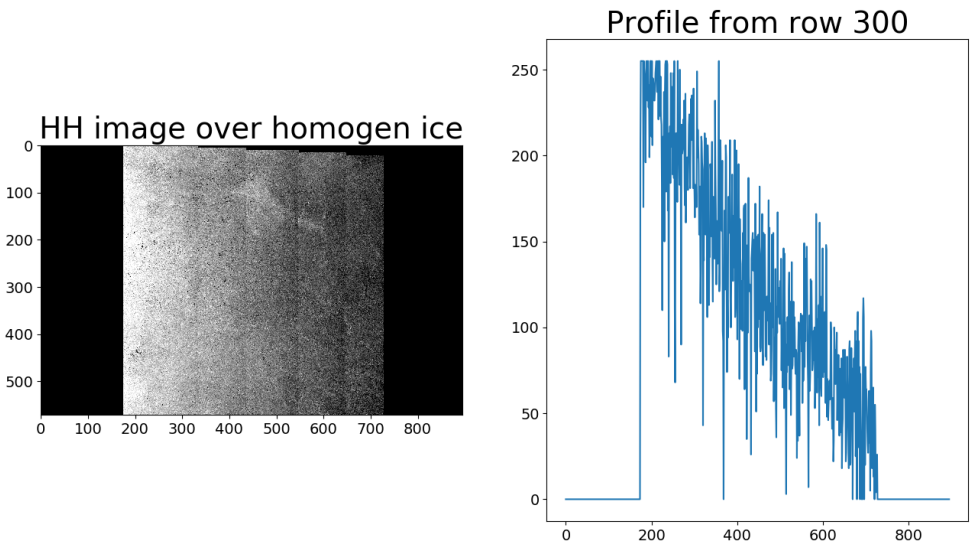

Figure 2.1: Incident angle effect and profile of digital values
Left: S-1 HH image over area with homogeneous ice. Right: Profile taken from near-range to far-range, showing a decrease in backscatter digital value to highlight ”The incident angle effect”. The profile is from row 300 in image to the left.

From a machine learning point of view the decrease creates over-segmentation and banding in the range direction, leading to a lower performance in real class distinction. In addition, different surface properties gives different intensity decay rates across range.

This has been dealt in the past by applying a global correction value for the whole scene[41; 25] or a manual correction per class[24; 29] in the preprocessing stage. For a global correction the results are improved, but leads to over correction for some areas and under correction for others. The manual way is tedious and time consuming and does not fit the frame for an automatic classification scheme.

The classifier used in this thesis includes the IA correction directly in the classification process. The method is introduced in [26] and explained in section 2.5

2.4 Standard techniques and theory

Section 2.4.2 is a review of chapter 2 in [40] and section 2.4.3 is a review of [8] (p. 539-542) and 2.4.4 is from (p.169-170) from the last mentioned author.

2.4.1 Technical tools

Python programming language is a an interpreted, high-level, object-oriented, cross-platform language and is consistently used throughout this thesis. Including, but not limited to, the use of search and download function for S-1 images(delivered by Centre for Integrated Remote Sensing and Forecasting for Arctic Operations (CIRFA)), use of estimating ice drift calculation, extracting and analysis of image information, statistical analysis, creation of figures in thesis, and more.

Sentinel Application Platform (SNAP) is an EO processing and analysis software, and in the combination with the S-1 Toolbox (S1TBX) is used for preprocessing of the images listed in A.1

2.4.2 Bayesian decision theory

In Bayesian decision theory the goal is to classify patterns in the most probable of classes.

A conditional distribution, $p(x|\omega_i)$, is describing a data set having affiliation to class ω_i, and $P(\omega_i)$ is the prior probability for the same class. By applying Bayes theorem, given samples x, we can find the posterior probability

$$P(\omega_i|x) = \frac{p(x|\omega_i)P(\omega_i)}{p(x)} \tag{2.1}$$

where $p(x)$ is the probability density function of x.

For a multiclass problem with M classes$(\omega_1, \omega_2, ..., \omega_M)$ the task is to find which class the sample x has the largest probability to belong to. Bayes classification rule for a multiclass problem states

$$x \in \omega_i \quad if \quad P(\omega_i|x) > P(\omega_j|x) \quad \forall \ i \neq j \tag{2.2}$$

In words, sample x is classified to class i if the probability for affiliation to class i is bigger than the probability for affiliation to any of the other classes.

By inserting 2.1 in 2.2 and by acknowledging that $p(x)$ is equal for all classes the decision rule can be stated as

$$x \in \omega_i \quad if \quad p(x|\omega_i)P(\omega_i) > p(x|\omega_j)P(\omega_j) \quad \forall \ i \neq j \tag{2.3}$$

The intersection between the conditional probability functions is the decision surface in the multidimensional feature space. Along this surface, classes (that are adjacent to this surface) are equal probable to happen. In this case, instead of working with probability, it is more mathematically convenient to work with equivalent functions of them. More precisely, a monotonically increasing functions called discriminant function, $g_i(x)$. Equation 2.3 is then written as

$$x \in \omega_i \quad if \quad g_i(x) > g_j(x) \quad \forall \ i \neq j \tag{2.4}$$

If the *a priori* probabilities, $P(\omega_i)$, for each class is equal then equation 2.3 is described as

$$x \in \omega_i \quad if \quad p(x|\omega_i) > p(x|\omega_j) \quad \forall \ i \neq j \tag{2.5}$$

and the result is the maximum likelihood classifier approach where

$$g_i(x) = p(x|\omega_i) \tag{2.6}$$

When statistical parameters needs to be estimated, maximization of the likelihood function is often used. This leads to whats known as “Maximum Likelihood Estimation”. From this the underlying pdf, that describes our data, can be built.

2.4.3 Simple Linear regression

Simple linear regression is an analysis of the functional dependence of one variable on another variable. The data consists of n pairs $(x_i, y_i), ..., (x_n, y_n)$, observations.

The relationship between the response variable, y, and the predictor variable, x, can be described with the linear equation

$$y_i = a + bx_i \tag{2.7}$$

The main purpose of regression is to predict the value of y_i based on value of x_i and when writing equation 2.7, the relationship between them is assumed to be linear, as the name of this section suggests.

a and $b$are unknown parameters and can be estimated with the following equations

$$b = \frac{S_{xy}}{S_{xx}} \qquad \text{and} \qquad a = \overline{y} - b\overline{x} \tag{2.8}$$

where S_{xx} is the sum of squares, S_{xy} is the sum of cross product and $\overline{x}$ and $\overline{y}$ are the sample means to the corresponding variable. The n paired observations will not settle exactly on a straight line, but the best fitted line will be the outcome and is called the regression line.

2.4.4 Correlation and covariance

Sometimes the strength of a relationship between parameters is of interest. This can be done by calculating the correlation coefficient, ρ, and is always in the interval [-1,1]. The endpoints in this interval, -1 and 1, are indicating a perfect linear relationship. If the correlation is positive it yields an upward trend, meaning if the predictor variable increases, the response variable does also. For negative correlation, an increase in response variable yields a decrease in the predictor variable. The closer the coefficient is to the endpoint the stronger the strength of relationship is. Coefficient that is zero indicate “no relationship” and the variables can be seen as random relative to each other.

Relationship can also be confirmed with the covariance between the same two variables, but does not directly give information about the strength. We still need the covariance to calculate the correlation coefficient:

$$Cov(X, Y) = E((X - \mu_X)(Y - \mu_Y)) \tag{2.9}$$

In equation 2.9, X and Y are variables, μ_X and μ_Y is the mean of X and Y

respectively while E denotes the expectation. We can now find the correlation of X and Y

$$\rho_{XY} = \frac{Cov(X,Y)}{\sigma_X \sigma_Y} \tag{2.10}$$

where σ_X and σ_Y in equation 2.10 is the standard deviation for X and Y, respectively.

2.5 Gaussian IA-classifier

The Gaussian Incident Angle (IA)-classifier is a supervised classification scheme that incorporates the IA variation across range. It does so by replacing the constant mean vector with a variable linear mean vector in a bayesian classifier, when a Gaussian distribution is assumed. The mean then becomes a linear function, in the log-space, dependent on the IA, θ.

The correction for IA is no longer a part of the preprocessing stage, but is incorporated in the training phase.

The "standard" Gaussian multivariate distribution

Every pixel intensity $\mathbf{x}$ is assigned to the most probable class ω_i. This is decided by the decision rule described in equation 2.5 for the Maximum Likelihood approach.

Here the $p(\mathbf{x}|\omega_i)$ is assumed to be the Gaussian multivariate class-conditional probability density function for ω_i. This is described by a mean vector, $\mu_\mathbf{i}$, and a covariance matrix, $\Sigma_\mathbf{i}$. The equation for a multivariate Gaussian distribution, with a constant mean vector, is

$$p_i(\mathbf{x}|\omega_i) = \frac{1}{(2\pi)^{\frac{d}{2}}|\Sigma_i|^{\frac{1}{2}}} e^{-\frac{1}{2}(\mathbf{x}-\mu_\mathbf{i})^T \Sigma_i^{-1}(\mathbf{x}-\mu_\mathbf{i})} \tag{2.11}$$

where d is the dimensionality of $\mathbf{x}$ and T denotes the transpose operation for a matrix.

The "Gaussian IA-classifier" multivariate distribution

In the case of the Gaussian IA-classifier the mean vector, $\mu_\mathbf{i}$ is replaced with a linear variable mean vector $\mu_\mathbf{i}(\theta)$ dependent on θ:

$$\mu_\mathbf{i}(\theta) = \mathbf{a_i} + \mathbf{b_i} \cdot \theta \tag{2.12}$$

where intercept $\mathbf{a_i}$ and the slope $\mathbf{b_i}$ for each class is calculated during the learning phase. By doing so the variation with IA is not longer an image property, but is treated as a class property. By inserting equation 2.12 in 2.11, the Gaussian multivariate distribution for the IA-classifier is written as

$$p_i(\mathbf{x}, \theta|\omega_i) = \frac{1}{(2\pi)^{\frac{d}{2}}|\Sigma_i|^{\frac{1}{2}}} e^{-\frac{1}{2}(\mathbf{x}-(\mathbf{a_i}+\mathbf{b_i}\cdot\theta))^T\Sigma_i^{-1}(\mathbf{x}-(\mathbf{a_i}+\mathbf{b_i}\cdot\theta))} \tag{2.13}$$

Covariance is now calculated as the mean squared deviation in respect to a mean value dependent to IA. By replacing the global constant mean vector with a linear variable mean vector we achieve a lower covariance.

By including equation 2.13 in the bayesian decision rule, described in equation 2.5, we get the Maximum Likelihood decision rule for the Gaussian IA.classifier.

In the study that introduces the Gaussian IA classifier, a total number of 9 classes is introduced. These classes are based on manual interpretation of overlapping optical and SAR data. For the work in this thesis, we use a version of the classifier that has reliably been trained for only 6 of these 9 classes. An overview of the classes is given in Table 2.1

Table 2.1: Implemented classes in the Gaussian IA-classifier

Class number	Class name	Implemented
1	Open Water(calm)	No
2	Open Water(windy)	No
3	Leads with Open Water/Newly Formed Ice	Yes
4	Brash/Pancake Ice	No
5	Young Ice I	Yes
6	Young Ice II	Yes
7	Level First-Year Ice	Yes
8	Deformed First-Year Ice	Yes
9	Second-/Multi-Year Ice	Yes

3

Methods and techniques

This chapter describes how the IWD and S-1 images are prepared, aligned and compared. Choices regarding viewing distance, ice drift and how the two sources are merged before comparison are explained along with the statistical analysis.

3.1 Preparing the two sources: Ice Watch database and Sentinel-1 images

3.1.1 Ice Watch database

Observations from Ice watch database are open for everyone to use and can be accessed online at MET's web page[1]. At the time the author of this thesis started to prepare data from IWD there were 5696 observation divided in 52 registered cruises on the web page. Throughout the period, at least one new cruise has been registered and is not included in this thesis.

All observation details, with its 113 parameters, were downloaded and combined to one single csv-file. Empty observations were removed and the global

1. https://icewatch.met.no/

Latitude/Longitude projection was converted to Arctic research projection[2]. This because the IA classifier projects the classified S-1 images to the latter mentioned projection.

From the 113 parameters that can be registered in an observation, we have manually selected 13, which are listed in Table 3.1. The selection is based on a manual choice that allows for best comparison to the classes in the Gaussian IA classifier.

Table 3.1: Parameters investigated from Ice Watch Database

Parameter	**Description**
Date	YYYY-MM-DD HH:MM:SS UTC
LAT	Latitude decimal degrees
LON	Longditude decimal degrees
TC	Total Concentration
PT	Primary Ice Type
PPC	Primary Partial Concentration
Ptop	Primary Topography Feature Type
ST	Secondary Ice Type
SPC	Secondary Partial Concentration
Stop	Secondary Topography Feature Type
TT	Tertiary Ice Type
TPC	Tertiary Partial Concentration
Ttop	Tertiary Topography Feature Type

The primary-, secondary- and the tertiary Ice Type are defined as “from thickest(Primary) to thinnest(Tertiary) ice” while their topography is recorded as PTop, STop and Ttop, respectively.

The primary-, secondary- and the tertiary partial concentration is the concentration for the different ice types and should always sum up to the total concentration. Ice types is listed as one of the types in Table 4.3 under ’Ice Watch classes’

One single observation was divided into three sub-observation: (PT, PPC, PTop), (ST, SPC, STop) and (TT, TPC, TTop). This division of observations was the foundation used for statistical analyses when comparing IWD with the classified S-1 images.

2. WGS 84(EPSG:4326) positions were converted to WGS 84/North Pole LAEA Europe(EPSG:3575)

3.1.2 Sentinel-1 images

The source for EO data was Copernicus Open Access Hub. 52 S-1 images were downloaded, preprocessed and classified. The complete enumerated list of images can be seen in Table A.1. Images used for InSAR calculation can be seen in Table B.1 and B.2 under “InSAR pair”

The criterion for downloading images was that an observation from IWD should be contained in two or more S-1 images within a timespan of +/- 12 hours. This criterion was set such that the InSAR capabilities could be used to estimate the ice drift at a later point.

Thermal noise was removed from the images before radiometric calibration and multilooking in the spatial domain was applied(within a 3-by3 neighborhood). The last step was to convert the digital numbers to decibel value. The preprocessing was achieved by the use of SNAP software. Theory of each preprocessing step can be seen in 2.3.2

The preprocessed images were fed to the "Gaussian IA classifier", described in section 2.5, which yielded the classified images with 6 predefined classes as described in Table 2.1, and can be seen in Table 4.3 under “IA-classifier, Ice type name”.

An example showing HH and HV intensity, a false-color composite (R-HV, G-HH, B-HH) and the classified image is shown in Figure 4.3 Note that areas with completely open water are misclassified, as they are not included in the trained classes of the classifier. This does not affect the analysis in this work, since we are mostly looking at areas with high sea ice concentration, where open water should be captured by the“Leads" class.

For visual analysis and comparison, all images shown in this thesis are scaled to the same dynamic range.

3.2 Aligning the sources

3.2.1 Viewing distance and viewing box

To define the distance the observer can visually see, and come to his or hers decision regarding prevailing ice condition, a viewing distance had to be set. In [2] it is stated: "Ice is viewed within 1 nautical mile from the ship during a 10 minute observation period" (p. 4) while according to the ASSIST/IceWatch

protocol[3] the observation radius should be done around the ship for a radius of 1 kilometer. The latter mentioned distance is also the recommended distance from MET.

For the purpose of this investigation, we decided to use a 2 by 2 kilometers box around the observation. This is well within the area that should be considered for the Ice Watch observation. Using Figure 4.4 as an example we can see the location of the observation as a blue dot in the middle. The distance from the blue dot to the top, bottom, left and right is approximately 1 kilometer. To the corners the distance is 1.4 kilometers. The chosen viewing box will therefore be a combination between the two sources for viewing distance

3.2.2 Estimating ice drift

By the use of InSAR capabilities of S-1 an estimate for drift could be calculated for each observation. This is done by the use of NERSC's sea ice drift from Sentinel-1 software[4]. As stated it is a "computationally efficient, open source feature tracking algorithm" written in the programming language Python 3.6 [22; 31; 27]

By comparing two S-1 images over the same geographical area, that only deviates in time, the feature tracking algorithm is able to quickly and efficiently estimate a first guess of ice drift in a few unevenly distributed key points, and the pattern matching provide drift vectors on a regular or irregular grid. The result is ice drift vectors as seen in Figure 4.8 and 4.9.

The ice drift vector closest to observation extracted from IWD was used as drift estimate for that single observation. From this point two scenarios was tested:

Scenario 1: Use only observation that has ice drift less than 500 m in the proximity. No drift is applied

Scenario 2: Use all observation regardless of ice drift distance. Drift correct all observation

The 500 meter limit was chosen since this is half the viewing distance. With this it is assumed that the drift can be disregard since most of the pixel in the viewing box will remain the same.

Other sources for estimating ice drift was also considered. OSI-405-c and OSI-

3. https://icdc.cen.uni-hamburg.de/1/daten/cryosphere/seaiceparameter-shipobs/
4. https://github.com/nansencenter/sea_ice_drift

407-a from OSI SAF[5] is an option when investigating sea ice drift. The first mentioned sensor is a passive microwave and gives a 62.5 km resolution with 48 hour window. The product is too coarse to give reliable result. The latter is an optical sensor at 20 km resolution with 24 hour window. This will give a to sparse results due to cloud cover.

The pattern matching algorithm was not applied due to that it only produced invalid results. Investigating ice drift was not the main goal of this thesis and was therefore not a priority. An estimate is achieved by the use of feature tracking and the drift results can be seen in Table B.1 and B.2 under "Tot drift" for the total ice drift for scenario 1 and scenario 2, respectively

3.2.3 Merging and shifting the sources:

To compare the observation from IWD with the classification result from the IA-classifier these sources needed to be combined. IWD has 15 different ice types defined in addition to 'Open Water'. These ice types are given a value between 10 and 85. The IA-classifier has nine classes where only six are implemented: 3, 5, 6, 7, 8 and 9, as seen in Table 2.1.

To compare the results from both sources, ice types from IWD is merged down to six classes and shifted between the value of one to six. Classification results are also shifted such that values are no longer between three and nine, but also one to six.

Further the recorded topography from IWD is used to separate "Level-" and "Deformed First-Year ice". The First Year observations that did not contain reports of topography were not possible to clearly separate between the two classes 4 and 5. For statistical convenience this was set to class 4.5 with the motivation that the sum of many observations, between these two classes, will converge towards a value of 4.5. This way the statistical analysis would give the most realistic image as possible.

Results of the merging and shifting are listed in Table 4.3 along with the explanation to classes from both sources(class 4.5 is neglected from this table).

5. http://osisaf.met.no/status/

3.3 Comparing the sources

The correlation was investigated between IWD and the classified S-1 images to investigate if there is an association between these two sources and the relationship is modeled with linear regression as described in 2.4.3 and 2.4.4.

The thickest ice(Primary Ice Type) reported in IWD was compared to the thickest class yielded by the classifier. The second thickest(Secondary Ice Type) from IWD was compared to the second thickest class yielded by classifier. The third thickest from IWD was compared to the third thickest class yielded by classifier. This was done consistently and with no regards to the their corresponding partial ice concentration.

When looking at correlation and linear regression for the ice types, all valid sub-observations were used. But when investigating the concentration, only sub-observations which had ice types correctly set by the classifier, according to reported in IWD, was used. This since there was no reason to test for correlation for something that had already been proven wrong.

Overall comparison of valid sub-observations of scenario 1 and scenario 2 is shown in section 4.6.4. The reported observation from IWD and the result from the classifier is presented in the same histogram for both scenarios. This gives an impression how the class representatives for each class is spread throughout the whole dataset before classification, as well as how they are mapped during the classification process.

4

Results and discussion

The results of comparing IWD data with the Gaussian IA-classifiers results are shown in this chapter. From section 4.2 through section 4.4 the InSAR pair (34, 35) from Table A.1 and its corresponding observation is shown as an example, but was not included in any of the scenarios. This is shown for visual impression of how this investigation is conducted for all pairs listed in Table B.1 and B.2.

4.1 Results of extracting observation from Ice Watch database

As mentioned in chapter 3, IWD contains 5696 observation in the timespan 5. of August 2006 to 1. of August 2019. The number of observations per year and per month is shown in in Figures 4.1 and 4.2, respectively.

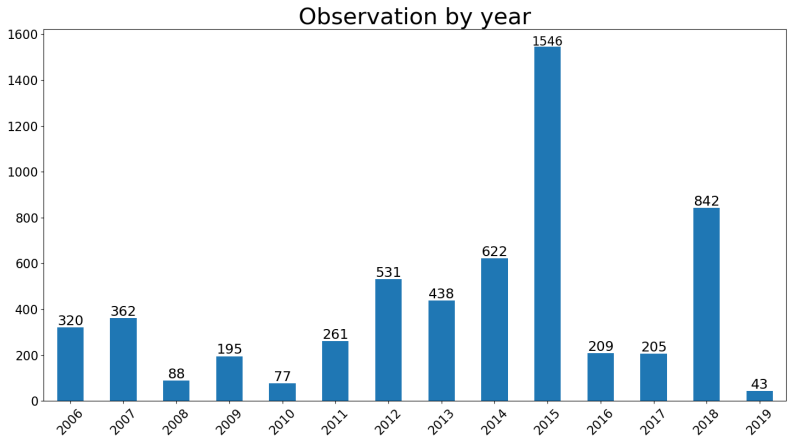

Figure 4.1: Observations from Ice Watch database by year
Number of observations registered in the Ice Watch database between 2006 and 1. of August 2019 by year

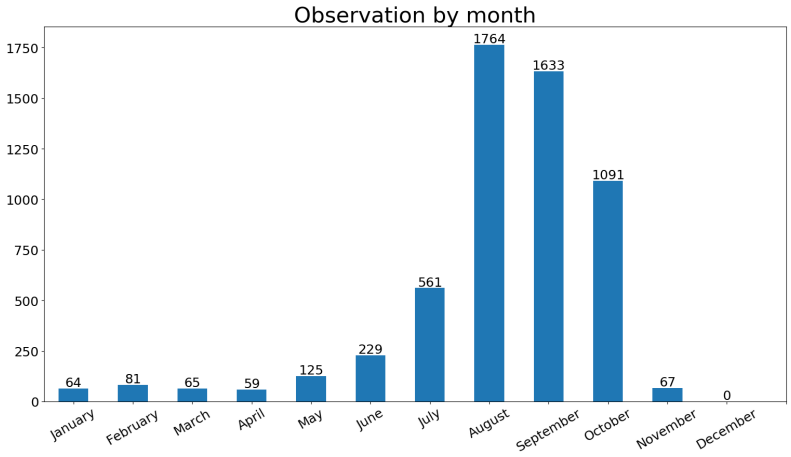

Figure 4.2: Observations from Ice Watch database by month
Number of observations registered in the Ice Watch database between 2006 and 1. of August 2019 by month

The years with most observations were 2015 and 2018 with 1546 and 842 registered on IWD, respectively. The monthly timespan with the highest count is from August to October, and holds a total of 4488 observations. The sea ice minimum marks the end of the melting season and usually occurs in this period[1].

1. https://cryo.met.no/en/arctic-melt-2019

This shows that most Arctic cruises that are conducting ice watch observations are taking place in the summer months. Using the IWD as validation for ice type classification may therefore be biased towards summer months, while at the same time, most automated ice type classification algorithms are tuned for winter/freezing conditions.

4.2 Classification results

Figure 4.3 shows subplots of example S-1 image 34 from Table A.1. “HH” and “HV” are the preprocessed product acquired from S-1 in EW. The “False color composite” is an RGB image consisting of HV in red channel and HH in both green and blue channel. The result of the Gaussian IA-classifier is shown as the “Labeled” sub-image.

Note that the Gaussian IA classifier in its current implementation disregards the entire first swath EW1 of the S-1 image. The first swath is particularly affected by the noise in the HV component, which may cause too much misclassification. It is therefore not processed by the current version of the classifier.

S-1 images acquired in EW have a spatial extent of 400 km. A consequence of this is that what looks like a blue dot is really two blue dots almost on top of each other. These two represent the position where the observation from IWD was reported. For a closer look at the area around the two observations see Figure 4.4 and 4.5. The closeup area correspond to the viewing distance explained in section 3.2.1

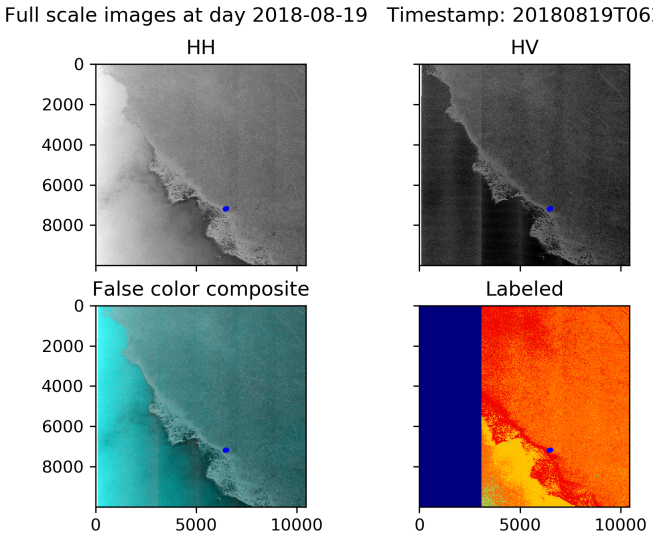

Figure 4.3: Full scale image of HH, HV, False color composite and labels
Example of an S-1 image containing two observation within a timespan of pluss/minus one hour. ”Timestamp” is the start-sensing-time for the S-1 image. Top left: HH. Top right: HV. Bottom left: False color composite with HV in red channel and HH in green and blue channel. Bottom right: Classification result indicating different ice classes using the color code explained in Table 4.3

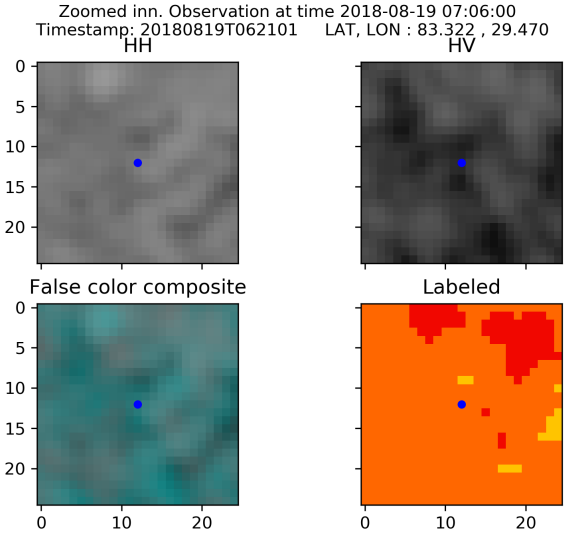

Figure 4.4: Example observation one
Closeup of S-1 image (HH, HV, false-color, labels) around observation 1/2 from Figure 4.3. The observation location is indicated by the blue dot and the images is cropped to a 25-by-25 pixel region around it.

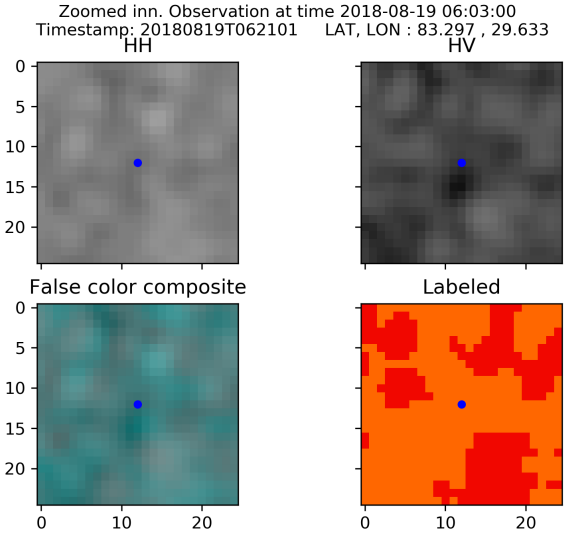

Figure 4.5: Example observation two
Closeup of S-1 image (HH, HV, false-color, labels) around observation 2/2 from Figure 4.3. The observation location is indicated by the blue dot and the images is cropped to a 25-by-25 pixel region around it.

4.3 Comparing observations with classification results

Figures 4.6 and 4.7 are the normalized histograms of the labeled sub-images of Figure 4.4 and 4.5, respectively. The parameters used to distinguish the type of ice and concentration from Table 3.1, for this particular observation, are included in the top left corner. Concentration are given in tenths.

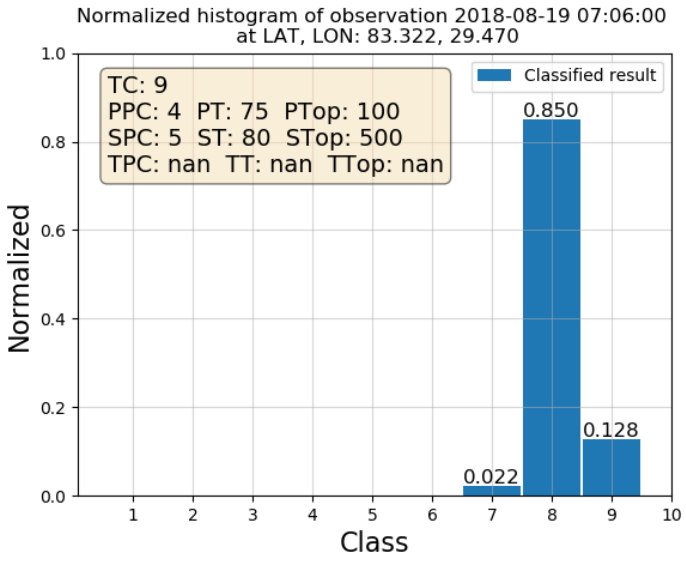

Figure 4.6: Example observation one - Histogram
Histogram of observation from labeled image in Figure 4.4. The box in the top left corner is observation data from IWD. The x-axis shows the classes from IA-classifier before shifting and merging. The y-axis is normalized.

Table 4.1: Comparing observation 1

Values from IWD and IA-classifier for observation corresponding to Figure 4.4 and 4.6. Concentration for IA-classifier is retrieved from the normalized histogram and is rounded to closest tenth. This observation yields two sub-observation.

Ice type and concentration	Observer from IWD	Classification results
Primary Ice Type	Second Year(75) Level Ice(100)	Second-/Multi-Year Ice(9)
Primary Partial Concentration	$\frac{4}{10}$	$\frac{1}{10}$
Secondary Ice Type	First Year >120cm(80) with Ridges(500)	Deformed First-Year Ice(8)
Secondary Partial Concentration	$\frac{5}{10}$	$\frac{9}{10}$
Tertiary Ice Type	NaN	Level First-Year Ice(7)
Secondary Partial Concentration	NaN	$\frac{0}{10}$

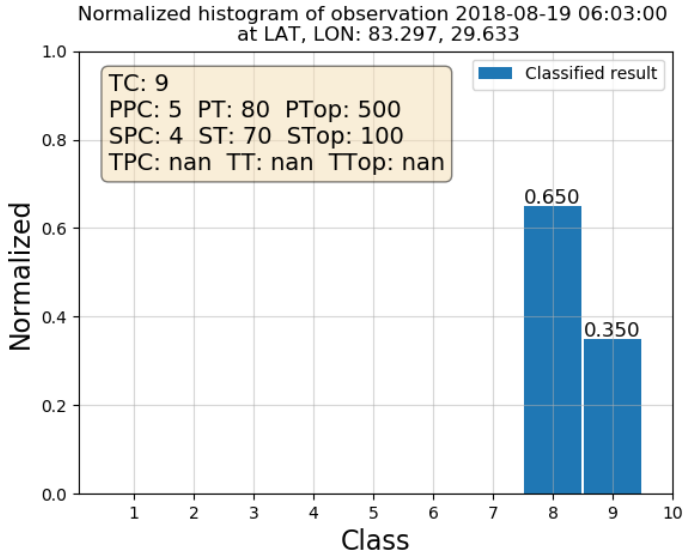

Figure 4.7: Example observation two - Histogram
Histogram of observation from labeled image in Figure 4.5. The box in the top left corner is observation data from IWD. The x-axis show the classes from IA-classifier before shifting and merging. y-axis is normalized

Table 4.2: Comparing observation 2

Values from IWD and IA-classifier for observation corresponding to Figure 4.5 and 4.7. This observation yields two sub-observation

Ice type and concentration	Observer from IWD	Classification results
Primary Ice Type	First Year >120cm(80) with Ridges(500)	Second-/Multi-Year Ice(9)
Primary Partial Concentration	$\frac{5}{10}$	$\frac{4}{10}$
Secondary Ice Type	First Year, 70-120cm(70) Level Ice(100)	Deformed First-Year Ice(8)
Secondary Partial Concentration	$\frac{4}{10}$	$\frac{6}{10}$
Tertiary Ice Type	NaN	NaN
Secondary Partial Concentration	NaN	NaN

4.4 Results of ice drift estimation

In Figure 4.8, the shown image and the red dotted box correspond to image number 34 and 35 in Table A.1, respectively. The keypoints calculated with the feature tracking algorithm can be seen as areas of red, scattered unevenly where the two S-1 images overlap. The keypoints represents drift in the area and are visualised as red arrows. A closeup around 2018-08-19 20:31:00 UTC can be seen in Figure 4.9

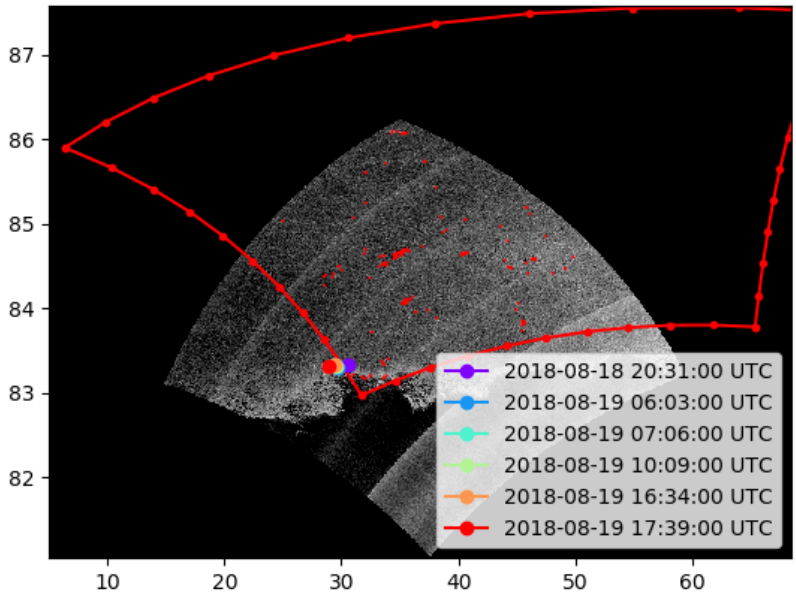

Figure 4.8: Drift calculation
Result after InSAR drift estimation by the use of feature tracking algorithm. Observations plus/minus twelve hours are plottet. The two observations seen in 4.3 correspond to date 2018-08-19 06:03:00 UTC and 2018-08-19 07:06:00 UTC. The red spots seen in the image are drift arrows indicating direction and speed estimates. For a closeup see Figure 4.9.

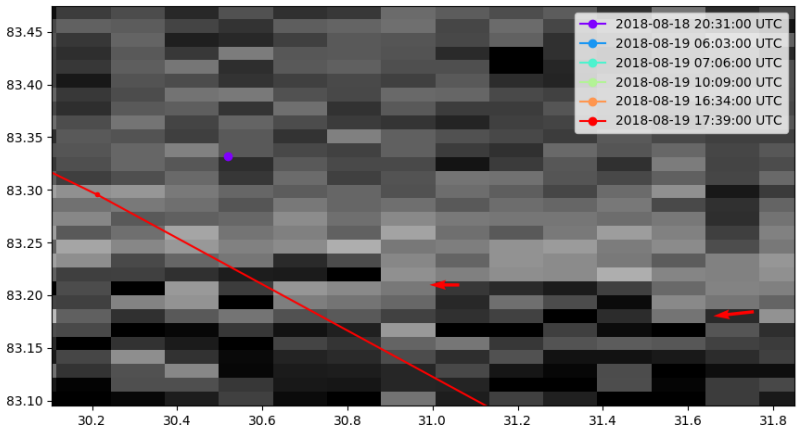

Figure 4.9: Drift calculation - Zoomed
Closeup near observation 2018-08-19 20:31:00 UTC from Figure 4.8. The red arrows are drift vectors calculated by the feature tracking algorithm.

4.5 Results of merging and shifting Ice Watch observations and classification results

Table 4.3 gives an explanation of how the shifting and merging of the data is performed. Ice Watch classes which are marked with the same color is merged to the same class and is given the “New merged class value.” IA-classifier labels holding the same color are shifted to the same “New merged class value”.

Table 4.3: Redefined classes after merging and shifting

Initial class values from Ice Watch database and IA classification class values and how they are merged to "New merged class values" for comparison. To separate class 4 and 5 in the "New merged class value", topography of the ice from ice watch database is used. This is seen as number 100(Level ice) or 500(Ridges) in parenthesis under "ice type value" for "Ice Watch classes"

Ice Watch classes		IA classifier		New merged class value
Ice type name	Ice type value	Ice type name	Ice type value	
Open Water	10	Leads with open water/Newly formed ice	3	1
Frazil	10			
Shuga	11			
Grease	12			
Slush	13			
Nilas	20			
Pancakes	30			
Young Grey Ice 10-15cm	40	Young Ice I	5	2
Young Grey Ice 15-30cm	50	Young Ice II	6	3
First Year < 70cm	60(100)	Level First Year Ice	7	4
First Year 70-120cm	70(100)			
First Year > 120cm	80(100)			
First Year < 70cm	60(500)	Deformed First-Year ice	8	5
First Year 70-120cm	70(500)			
First Year > 120cm	80(500)			
Second Year	75	Second/Multiyear	9	6
Multiyear	85			

4.6 Results of comparing the Ice Watch Database with classification results

Linear regression and the correlation between observations from IWD and classification results for both scenarios are shown in this section. This is done

for ice type and for ice concentration. Scenario 1 uses only observations that have an estimated drift less than 500 meters in the time interval between observation and S-1 sensing-start-time. The drift is not applied for this scenario. Scenario 2 applies the estimated drift for all observations.

Many observations hold the same values and are therefore plotted on top of each other. This is represented as numbers in plots, showing the amount of observations overlapping each other. The values on the x- and y- axes are described in section 3.2.3 and shown in Table 4.3 under "New merged class values." The new class values can be interpreted that it holds the same ice type as IA-classifier ice type. E.g. the new class value 6 corresponds to "Second/Multiyear" for both IWD observations and classification results.

4.6.1 Scenario 1: No drift comparison

Ice Type

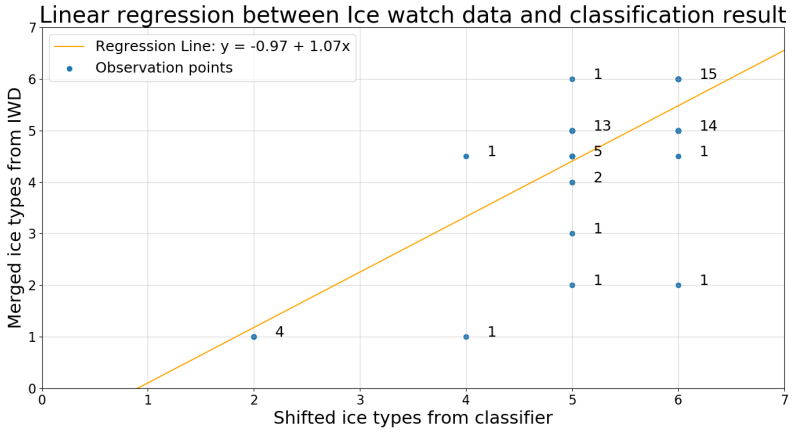

Figure 4.10: Linear regression without drift - Ice type

Scatter plot of classification results versus observations from IWD. The shifted IA-classifier ice type classes on the x-axis. The merged ice type classes from IWD on the y-axis. Regression line between these two variables is drawn and corresponds to y = -0.97 + 1.07x. The number placed next to the observation show how many observations plotted on top of each other

Correlation matrix, Ice type

$$\begin{bmatrix} 1 & 0.79696823 \\ 0.79696823 & 1 \end{bmatrix}$$

Scenario 1 for ice types yields a regression line given by y = -0.97 + 1.07x. The correlation between observations from IWD and classification results is 0.80.

From the correlation matrix we can see a medium/large positive association(0.79696823) between IWD and classification result. High value observations in field corresponds to a high classification result and is confirmed by the regression line. 28 of the 60 sub-observations are correctly set to the same ice types according to IWD. This gives an overall accuracy of 46.7 %. Observation details are given in Table B.1.

Table 4.4: Confusion matrix - Scenario 1

Confusion matrix for scenario 1 from Figure 4.10 Intermediate class 4.5 excluded. ACC is the per class accuracy.

		Ice Watch database					
		Class 1	Class 2	Class 3	Class 4	Class 5	Class 6
IA-classifier	Class 1						
	Class 2	4					
	Class 3						
	Class 4	1					
	Class 5		1	1	2	**13**	1
	Class 6		1			14	**15**
	ACC	0	0	0	0	0.481	0.938

Table 4.4 shows the per class accuracy when the intermediate class 4.5 is excluded. This gives 48.1 % accuracy for class 5 and 93.8 % accuracy for class 6. Class 1-4 have 0 % accuracy. When the intermediate class (class 4.5) is excluded an overall accuracy of 52.8 % is achieved.

Sea ice Concentration

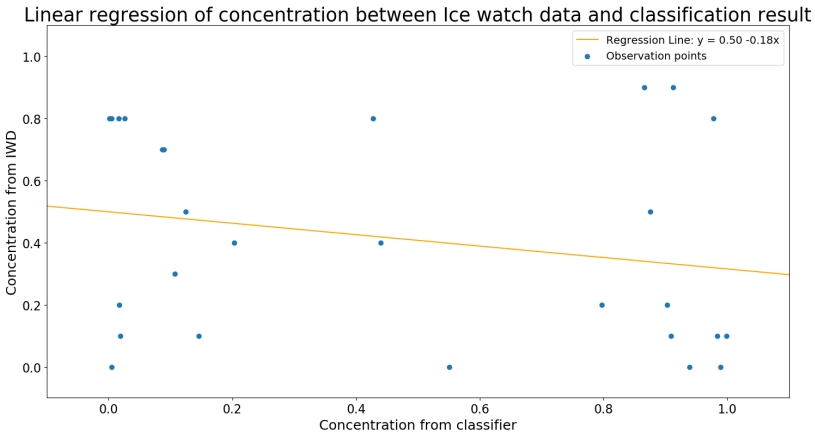

Figure 4.11: Linear regression without drift - Concentration
Scatter plot of classification concentration versus concentration from IWD. Concentration from classifier on the x-axis. Reported concentration from IWD on the y-axis. Regression line between these two variables is drawn and correspond to y = 0.50 - 0.18x. Only the 28 sub-observations correctly classified, is used

Correlation matrix, Concentration

$$\begin{bmatrix} 1 & -0.22995975 \\ -0.22995975 & 1 \end{bmatrix}$$

Scenario 1 for concentration yields a regression line given by y = 0.50 -0.18x. The correlation between observations from IWD and classification results is -0.23. The 28 correctly classified sub-observations are used in this calculation.

From the correlation matrix for concentration we can see a small negative correlation between IWD and classification result. High value for concentration in field correspond to a lower classification value for concentration.

4.6.2 Scenario 2: With drift comparison

Ice Type

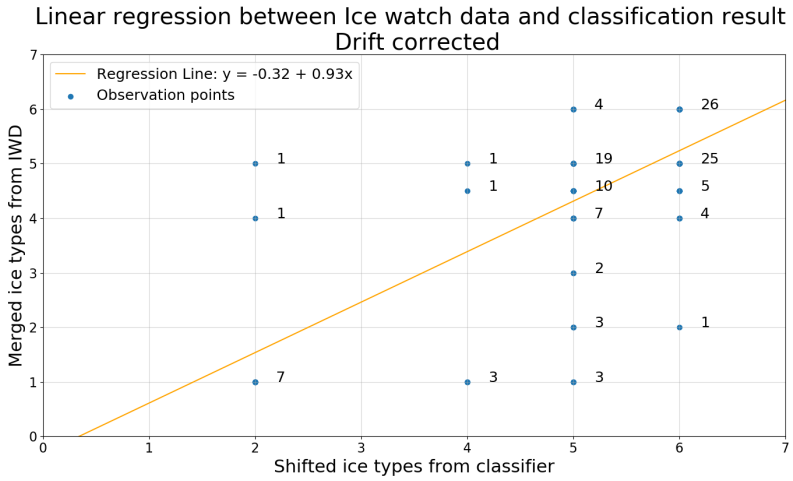

Figure 4.12: Linear regression with drift correction - Ice type

Scatter plot of classification ice type versus ice type from IWD. Ice type from classifier on the x-axis. Reported ice type from IWD on the y-axis. Regression line between these two variables is drawn and correspond to y = -0.32 + 0.93x. The number placed next to observation shows how many observations plotted on top of each other.

Correlation matrix, Ice type

$$\begin{bmatrix} 1 & 0.66578677 \\ 0.66578677 & 1 \end{bmatrix}$$

Scenario 2 for ice types yields a regression line y = -0.32 + 0.93x. The correlation between observation from IWD and classification results is 0.67.

From the correlation matrix we can se a medium positive association(0.66578677) between IWD and classification result. high observation in field correspond to a high classification result. 45 of the 123 sub-observation is correctly set to the same ice types according to IWD. This yields an overall classification accuracy on 36.7%. Observation details can be seen in B.2

Table 4.5: Confusion matrix - Scenario 2

Confusion matrix for scenario 2 from Figure 4.12 Intermediate class 4.5 excluded. ACC is the per class accuracy.

		Ice Watch database					
		Class 1	Class 2	Class 3	Class 4	Class 5	Class 6
IA-classifier	Class 1						
	Class 2	7				1	
	Class 3				1		
	Class 4	3				1	
	Class 5	3	3	2	7	**19**	4
	Class 6		1		4	25	**26**
	ACC	0	0	0	0	0.413	0.867

Table 4.5 shows the per class accuracy when the intermediate class 4.5 is excluded. This gives 41.3 % accuracy for class 5 and 86.7 % accuracy for class 6. Class 1-4 have 0 % accuracy. When the intermediate class is excluded this gives an overall accuracy on 42.1 %

Ice Concentration

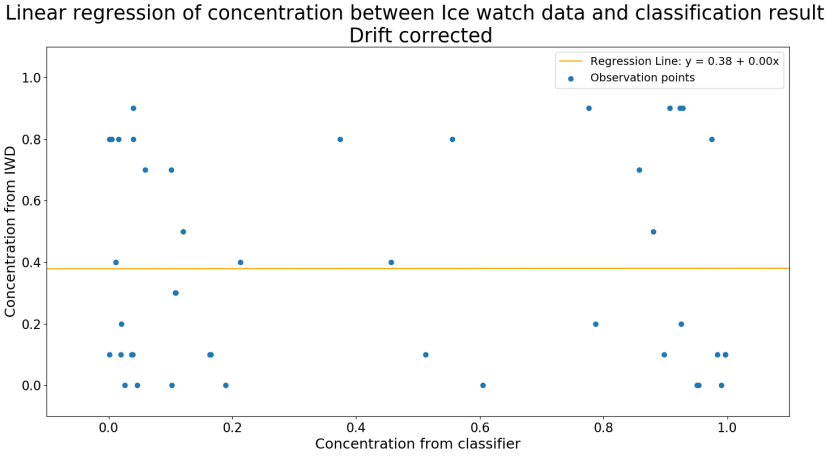

Figure 4.13: Linear regression with drift correction - Concentration

Scatter plot of classification concentration versus concentration from IWD. Concentration from classifier on the x-axis. Reported concentration from IWD on the y-axis. Regression line between these two variables is drawn and correspond to y = 0.38 + 0.00x. Only the 45 sub-observations correctly classified, is used.

Correlation matrix, Concentration

$$\begin{bmatrix} 1 & 0.00140065 \\ 0.00140065 & 1 \end{bmatrix}$$

Scenario 2 for concentration yields a regression line given by y = 0.38 + 0.00x. The correlation between observations from IWD and classification results is 0.00. The 45 correctly classified sub-observations are used in this calculation.

From the correlation matrix for concentration we can see a neglectable small correlation between IWD and classification result.

4.6.3 Correlation hour by hour for ice types

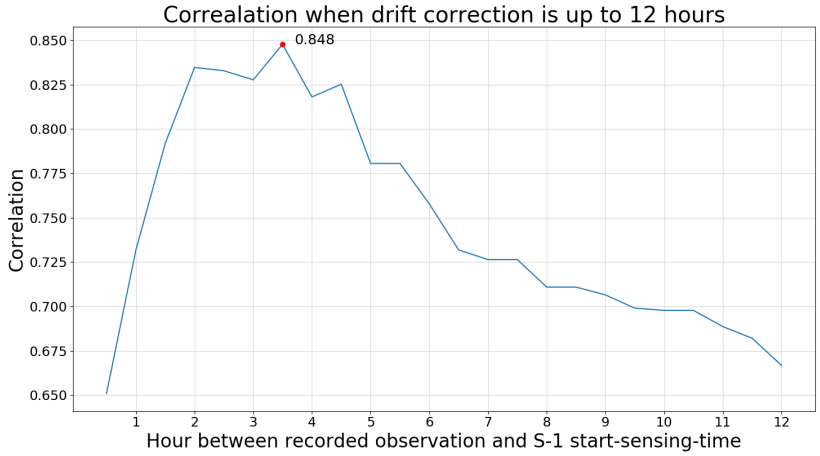

Figure 4.14: Overall correlation for ice types

Plot of the correlation between reported ice types from IWD and ice types yielded from classifier when drift correction is applied. x-axis shows hours between recorded observation and S-1 start-sensing-time. y-axis shows the correlation. The red dot indicates the highest correlation for this dataset. This occurs after 3.5 hours and the correlation is 0.848

Figure 4.14 shows that the correlation is increasing to a value of 0.848 after 3.5 hours before starting to drop to a value of 0.67. For 12 hours all the 123 sub-observations are included. When moving left towards zero time difference, less observations are included.

4.6.4 Overall comparison

In Figures 4.15 and 4.16 the complete data sets for scenario 1 and scenario 2 are shown, respectively. The classes are separated on the x-axis while y-axis is normalized such that the total height of the bars from each source add up to 1 and can easily be interpreted as percentage.

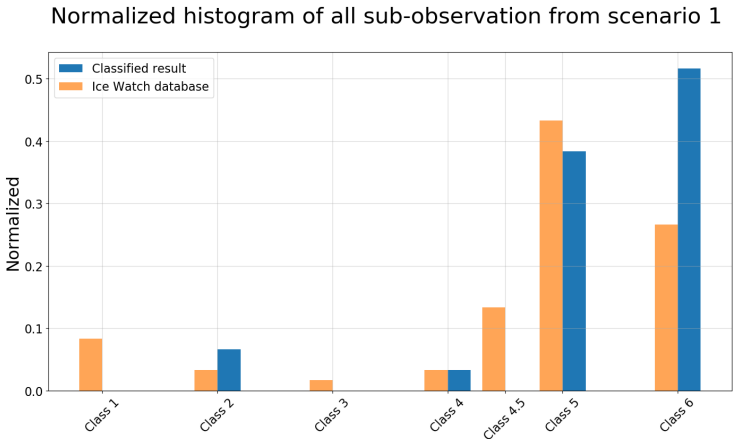

Figure 4.15: Overall comparison - Scenario 1

Histogram of valid sub-observations from scenario 1 seen in Figure 4.10 and Table B.1. Classes corresponding to Table 4.3 under "New merged class value" on the x-axis. Normalized y-axis. "Ice Watch database" is the reported observations from IWD. "Classification result" is the result yielded from the IA-classifier.

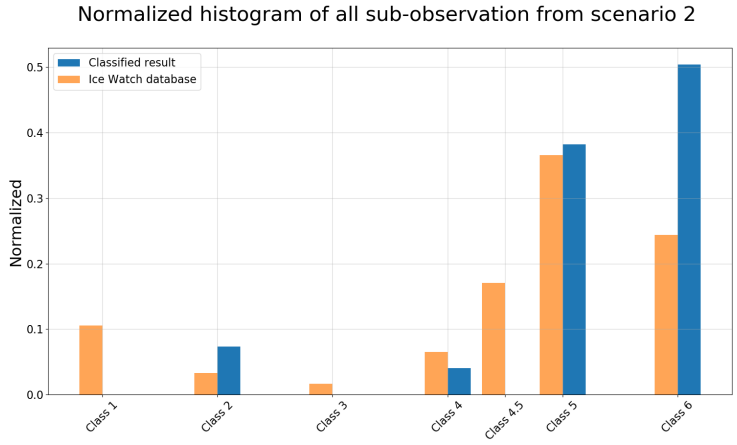

Figure 4.16: Overall comparison - Scenario 2

Histogram of valid sub-observations from scenario 2 seen in Figure 4.12 and Table B.2. Classes corresponding to Table 4.3 under "New merged class value" on the x-axis. Normalized y-axis. "Ice Watch database" is the reported observations from IWD. "Classification result" is the result yielded from the IA-classifier.

Both Figures 4.15 and 4.16 show low representation of sub-observations for classes 1-4.5. Most of the observations reported in IWD are contained in class 5 and 6.

4.7 Discussion

In total, the 52 S-1 images used in this thesis contain 148 of the 5696 available observations in the IWD. Most of these observations are from the years 2015 and 2018. These are also the two years with the most overall observations within the IWD (see Figure 4.1).

Scenario 1: No drift correction

Ice type:
After removing observations with drift above 500 m, we are left with 76 observations. Five of these 76 were removed because they did not contain all required parameters. Of the 71 remaining observations only 37 are still in the image after the classifier has masked out the first swath EW1. Each of the 37 observations have up to three sub-observations. Total numbers of sub-observations included is 60.

After applying linear regression between IWD observations and classification results the regression line y = -0.97 + 1.07x was obtained. The correlation between these variables was 0.80.

The correlation gives a statistical medium to large positive association between these two variables. This indicates that the relationship between IWD and the result from the Gaussian IA-classifier is significant and not random. We can expect that if an observer see thick ice in the field the classifier will yield thick ice.

28 of 60 was correctly classified according to IWD which yields a total classification accuracy of 46.7%. When not taking into account the intermediate class 4.5 in the confusion matrix, the overall accuracy increased to 52.8 %. This was expected since class 4.5 only applies to IWD. A consequence of this was that this class does not map to any classes in the IA-classifier and was therefore removed from the confusion matrix, giving a higher true positive. Class 4.5 was included for the sake of correlation and regression.

Sea ice concentration:
For sea ice concentration the correlation(-0.23) yields a weak negative correlation. Looking at the regression line, y = 0.50 -0.18x, in Figure 4.11 we

can see a decrease in the concentration yielded from classifier when the reported concentration from IWD increases. This is the opposite of what was expected.

Scenario 2: With drift correction

Ice type:
Eight of the totally available 148 observations for this scenario were removed because they did not contain all required parameters. After removing all observations in swath EW1 as well, a total number of 75 valid observations remains. The total number of sub-observations is 123.

The linear regression for scenario 2 gave the regression line y = -0.32 +0.93x and the correlation between IWD and IA-classification result was 0.67.

Including the drift correction gave a medium positive association between these two variables. In the same manner as for scenario 1 we can conclude that there is a relationship, even after drift correction. However the relationship is weaker. This is most likely due to that with drift correction we include more observations that has to be shifted geographically, and the time deviation is larger between observation time and S-1 start-sensing time. The drift is assumed to be constant in speed and direction no matter the time deviation. In reality this will vary and is therefore a source for error which is not accounted for. E.g. one of the observation for InSAR pair (13, 14) is drift corrected over 14 kilometers and the time deviation is over 11 hours. For this particular observation the primary and the secondary ice type did not match as seen in Table B.2. The advantage of using drift corrected values, even though the correlation decreases, is that we include more observations giving the scenario a higher statistical value.

45 of 123 was correctly classified according to IWD which yields a total classification accuracy of 36.7%. When not taking into account the intermediate class 4.5 in the confusion matrix, the overall accuracy increased to 42.1 %. The per class accuracy for class 5 and 6 was 41.3% and 86.7%, respectively. These classes correspond to “Deformed First Year Ice” and “Second-/Multiyear”. A slightly higher result was also achieved for scenario 1: 48.1% and 93.8% for class 5 and 6. Again, this is expected due to incorporation of ice drift in scenario 2. For classes 1-4 the per class accuracy was 0% for both scenarios.

Sea ice concentration:
The regression line for ice concentration can be seen in Figure 4.13 and was y= 0.38 + 0.00x. The correlation was 0.00. No association was found between concentration reported in IWD and concentration yielded by classifier when including drift correction.

Correlation hour by hour

Figure 4.14 shows that the correlation first increases with time difference and reaches a value of 0.848 at 3.5 hours, before decreasing to a value of 0.67 after 12 hours. For 12 hours deviation we include more datapoint, but as the time passes these points become more and more inaccurate. This is a trade-off between larger numbers of data points and low time deviation. For this dataset, the highest correlation is achieved after 3.5 hours. The value of 0.848 indicates a strong positive correlation.

General discussion and summary

For both scenarios we achieved similar results. For ice types, the correlation is achieved between IWD observations and results obtained from the IA-classifier. Scenario 1 yielded a stronger correlation than scenario 2. The strongest association occurred when including drift and observations within a timespan of 3.5 hours as seen in Figure 4.14.

Correlation for sea ice concentration was weakly negative for scenario 1 and close to zero for scenario 2. The expectation was higher reports of sea ice concentration in IWD yields higher sea ice concentration from classifier. The result from scenario 1 was the opposite of the expected result, and the result from scenario 2 is telling us that the values from these two variables seem to occur by random from a statistical point of view. It can be difficult for humans to assess the concentration of ice from distance when observation is conducted at near-ground level. In addition, in the classification, the maximum likelihood chooses the class with the highest probability for each pixel, thus loosing the per-pixel fractions of ice. These factors may partially induce error in the sea ice concentration results. In the case of classification, in future investigation we can keep the per-pixel fractional likelihoods and calculate the average over all the pixel in the viewing box, and then compare this result to observations from IWD. This may improve the results regarding comparing sea ice concentration.

From both scenarios, 0% per class accuracy are reported for classes 1-4. Only class 5 and class 6 are partially set to the correct classes, as seen in Table 4.6. Most of the observations are done in heavily ice infested areas, resulting in fewer representatives for classes 1-4 from IWD. For scenario 1, classes 1-4 have only 10 of 60 sub-observations, while class 5 and 6 contains the remaining 50. The same can be said for scenario 2 with 31 sub-observations for classes 1-4 and 91 for class 5 and 6.

The best performing class was class 6 with a per class accuracy on 93.8 % and 86.7 % for scenario 1 and scenario 2, respectively. For class 5 it was 48.1 % and 41.3 % for scenario 1 and scenario 2, respectively. Even though classes 1-4 all

Table 4.6: Per class accuracy - Overview

Per class accuracy from confusion matrix. Scenario 1 and scenario 2

Class	Scenario 1	Scenario 2
1	0	0
2	0	0
3	0	0
4	0	0
5	48.1 %	41.3 %
6	93.8 %	86.7 %

ended up on 0 % accuracy. There were so few comparison points for these classes that no statistically significant conclusions can be drawn. More data is needed for classes 1-4.

When investigating the confusion matrix for scenario 1 for classes 5 and 6, we can see that observations in field corresponding to "Second/Multiyear" is mostly set to the same class by the classifier(15 of 16 observations) while roughly half of the observations corresponding to "Deformed First-Year Ice" is set to the correct class(13 of 27 observations). The same is true for scenario 2 where 26 of 30 observations from IWD are set correctly to "Second/Multiyear" and 19 of 46 observations from IWD are set correctly to "Deformed First-Year Ice." This result is valuable for those who travel in heavily ice infested areas where it is critical to separate the second year and multiyear ice from other ice types. This could, for instance, be an icebreaker capable of traveling in lighter ice condition but not the thicker ice types, industry that need reliable daily information about the presence of second/multiyear ice. Or any ship or entity, traveling in such area, wanting to avoid the risk of heavier ice for any reasons, such as saving fuel, finding a low risk route, conduct research in the area, and more.

The comparison for the statistical analysis was done in such a way that the thickest ice from IWD was consistently compared to the highest class yielded from the classifier, second thickest to second highest and third thickest to third highest, as explained in section 3.3. When doing this, the assumption "The classifier yields the same categories of ice as the observer" is drawn. This is not always the case. For the second example observations seen in 4.2 the Primary Ice Type from IWD is "First Year >120cm(80) with Ridges(500)." This was coupled with highest class yielded by the classifier "Second-/Multi-Year Ice(9)". Consequently this sub-observation was a mismatch. It was compared to class 6 while the right class would have been class 5 "Deformed First-Year Ice." In fact, the second thickest reported from the classifier was "Deformed First-Year Ice". Both sub-observations was mismatched in this example. By

a closer investigation of this particular observation we could have coupled the Primary Ice Type from IWD with the Secondary Ice Type yielded by the classifier and achieved at least one match. This is not done in this thesis, but performing such an investigation would increase per class accuracy, but not necessarily correlation.

Another approach of comparing, which was not conducted in this thesis, could be to merge the classes in Table 4.3 even more. Class 1 and 2 merged to class 1, class 3 and 4 merged to class 2, and class 5 and 6 merged to class 3. This would reduced the resolution regarding class distinction, but could potentially increased the accuracy for our "New class value" 1, 2 and 3. Class 1 representing "Open water and Newly formed ice less than 15 cm", class 2 representing "Level First Year Ice/Young ice > 15 cm" while class 3 representing "Deformed First-Year ice and Second-/Multiyear Ice". The overall accuracy then becomes 78 % for scenario 1 and 66 % for scenario 2. This could still be interesting for industry and shipping in the Arctic area for getting a rough overview of ice condition for area of interest.

Pixel size of S-1 images acquired in EW is 40-by-40 m. The preprocessing applied on S-1 images in this investigation had multilooking as one of the stages. This was done in the spatial domain with an averaging filter in a 3-by-3 pixel-neighborhood. The motivation for doing so is to remove noise, but at the same time all pixel values in the neighborhood are being mixed together, as explained in section 2.3.2 under "Multilooking". A consequence is that resolution for real class distinction is closer to 120-by-120 m. Often thinner ice appear in narrow leads and may be mixed together with thicker ice in the averaging process.

The IA-classifier yields one single class per pixel while observations from IWD can contain a mixture of several classes within the same pixel area. By looking at figure 4.10 and 4.12, the observations from class 1 in IWD "Leads with open water/Newly formed ice" are being classified to the thicker classes 2, 4 and 5. The observations from IWD, belonging to the lower classes(1-4), are "shifted" to the higher classes. This is partially an unwanted result from the multilooking and partially a result that the observer on ground simply can give a more detailed description of surface than the S-1 sensor. For both scenarios it is also important to notice the difference in class representatives from the IWD. Classes 1-4 has few observations while most observations is for class 5 and 6.

With a closer investigation of ice drift, a better result may be achieved. There are mainly two sources that induces uncertainty. In this thesis the rough linear estimation applied may be too inaccurate. Especially for values that deviate in time and spatial extent in an extreme fashion. This can be solved by removing

these outliers and only including observations that satisfy predefined maximum conditions regarding time and distance. The second source for error is that even though the time deviation is not extreme, observations that deviates equally in distance, but not in time, have equal impact on the result. E.g. an observation that has drifted 200 m the last 30 minutes is given equal importance as an observation that has drifted 200 m the last 5 hours. Increase in time will lead to a greater uncertainty. This could e.g. be solved with a weighted time penalty.

When merging the classes from IWD, 15 classes in addition to "Open Water" were reduced to six classes. This gives a lower resolution for the distinction of classes regarding IWD. Most of the classes were for thinner ice and since most of the observations were done in heavily ice infested areas this would have a minor effect. The merging needed to be done in order to compare these two sources. The shifting did not degrade the result.

Visibility was one of the mandatory parameters that must be registered when doing an IWD observation. For all observations it was assumed that there was good enough visibility so that the observation could be conducted within a 2-by-2 km box. This is true for 50 of the 75 observations in Table B.2. The remaining reported visibility below 1000 meters and will add some uncertainty to the results.

All observations from IWD is done by human interpretation of the prevailing condition of ice. In the database there is a total reported number of 213 different primary observers. Different skills, expertises and experience will vary from person to person and will include a bias to each observation. In addition, when reporting observations to the ASSIST software, "sloppy fingers" occur. E.g. the max value reported for the ships speed is 300 knots. This is highly unlikely. This specific error is easy to reveal, but smaller errors that might seem reasonable and logical can remain hidden in the dataset. In this thesis it is assumed that for all observations the reported details are correct and no bias is appended to any observers.

Regarding the ships speed, it is stated in the Ice Watch manual that an observation should be conducted during a 10 min period when the ship is in motion. It seems like this criterion has not been a priority. Many observations does not report ship speed. Many report 0 knots, indicating that observations are done when drifting with the ice. If this is so, the consequence is that the same ice is observed several times, despite this being discouraged by the manual. For this investigation it does not inflict any degradation of the results since we are comparing single observations to single geographical points. Nevertheless, it is a weak indication that not all observations are done consistently.

Many parameters are excluded from this study. For the parameters included, there were other parameter describing them in more detail that also were excluded. E.g. for the topography there exist parameters describing the concentration and height of the topography. This was not accounted for. Investigating a different set or including more of the 113 parameters can improve the results.

Other subjects not investigated/accounted for in this thesis

- Season variability: melting season vs freezing season
- Salinity variability and how it affects the dielectric properties of ice
- Geographical variability
- Different machine learning algorithms are not tested

5

Conclusion and future work

For this thesis, 52 Sentinel-1 images acquired in Extra wide swath mode were downloaded, preprocessed and classified with the "Gaussian IA-classifier", developed at the UiT. The classified images were compared to in-situ observation from the Ice Watch database to investigate wether the database can potentially be used as ground truth for a machine learning algorithm.

The results from the classified images were compared to 75 observations divided in 123 sub-observations from IWD. Two scenarios were investigated:

1. Use only observations that have ice drift less than 500 m in the proximity. No drift is applied

2. Use all observations regardless of ice drift distance. Drift correct all observations

For both scenarios, the correlation, regression line, and the confusion matrix were calculated.

In addition, overall comparison by investigating the correlation up to 12 hours when drift correction was applied, was done.

5.1 Conclusion

By the limitation and criteria set by this thesis a medium to strong correlation between ice types from the classified S-1 images and IWD was found. This is true for both scenarios. This indicates that there is a medium to strong association between the reported ice types from IWD and ice types yielded from the "Gaussian IA-classifier". When investigating ice concentration, a weak negative correlation for scenario 1 was found and no correlation was found for scenario 2.

The classifier was able to separate "Second/Multiyear ice" and "Deformed First-Year Ice". The per class accuracy for "Second/Multiyear ice" scored highest with 93.8% and 86.7% for scenario 1 and scenario 2, respectively. The per class accuracy for "Deformed First-Year Ice" was 48.1 % and 41.3 % for scenario 1 and scenario 2 respectively.

The classifier lacked the ability to correctly set "Level first Year Ice", "Young Ice II", "Young Ice I" and "Leads with open water/Newly formed ice". More observations, representing these classes, are needed.

Further more, the classifier segregates most of the "Second-/Multiyear Ice" and partially the "Deformed First-Year Ice". This is useful for industry, shipping and other with interest in the Arctic area, that finds information of separation of thicker ice from thinner ice, interesting.

The investigation performed in this thesis demonstrates the potential of the Ice Watch database to be used as ground truth for a machine learning algorithm for sea ice classification. Including more observations and re-grouping the trained classes will give a coarser class distinction, but can be used to give an improved overview of the entire Arctic region.

5.2 Future work

Implementing a classification scheme with equal classes as defined in [2] in addition to including more parameters from the same manual would give a more realistic mapping between IWD and SAR imagery.

S-1 images are strongly affected by noise, in particular in swath EW1. This leads to many valid observations being removed. Trying to connect other sensors where this is not an issue will give data more points for comparison and will increase the statistical value of the investigation.

EO data for S-1 is free to use and more images and observations can be included in the future to achieve more comparison points.

Comparing SAR images with high spatial resolution to IWD can “close the gap” between the resolution difference between in situ and SAR observations.

Appendices

A

List of S-1 images

Table A.1: List of S-1 images

Enumerated list of Sentinel-1 images investigated in this thesis. Sorted by date.

Nr.	Image name
1	S1A_EW_GRDM_1SDH_20150209T064622_20150209T064722_004543_00594C_4F01
2	S1A_EW_GRDM_1SDH_20150209T082436_20150209T082536_004544_005951_B2D9
3	S1A_EW_GRDM_1SDH_20150223T130146_20150223T130246_004751_005E31_51B1
4	S1A_EW_GRDM_1SDH_20150223T144029_20150223T144129_004752_005E35_6245
5	S1A_EW_GRDM_1SDH_20150307T062950_20150307T063050_004922_006256_63C3
6	S1A_EW_GRDM_1SDH_20150307T080804_20150307T080904_004923_006261_3B96
7	S1A_EW_GRDM_1SDH_20150310T065403_20150310T065503_004966_006374_D030
8	S1A_EW_GRDM_1SDH_20150310T083245_20150310T083345_004967_00637B_3F44
9	S1A_EW_GRDM_1SDH_20150314T062145_20150314T062245_005024_0064CB_E8FB
10	S1A_EW_GRDM_1SDH_20150314T075952_20150314T080052_005025_0064D2_1C85
11	S1A_EW_GRDM_1SDH_20150315T070245_20150315T070345_005039_00652C_1BA8
12	S1A_EW_GRDM_1SDH_20150315T084057_20150315T084157_005040_006532_D6F8
13	S1A_EW_GRDM_1SDH_20150601T061431_20150601T061531_006176_0080A7_F1E5
14	S1A_EW_GRDM_1SDH_20150601T075158_20150601T075258_006177_0080AF_B494
15	S1A_EW_GRDM_1SDH_20150615T140809_20150615T140909_006385_0086BC_D3DD
16	S1A_EW_GRDM_1SDH_20150615T154626_20150615T154726_006386_0086C2_68BA
17	S1B_EW_GRDM_1SDH_20161005T165711_20161005T165811_002374_00402B_55E9
18	S1A_EW_GRDM_1SDH_20161005T174612_20161005T174717_013358_0154E7_19C6
19	S1A_EW_GRDM_1SDH_20170519T063105_20170519T063209_016647_01BA0A_4D44
20	S1B_EW_GRDM_1SDH_20170519T071938_20170519T072038_005664_009EB7_BA79
21	S1A_EW_GRDM_1SDH_20170520T071215_20170520T071319_016662_01BA7C_1C51
22	S1B_EW_GRDM_1SDH_20170520T080029_20170520T080129_005679_009F28_5485
23	S1B_EW_GRDM_1SDH_20170523T064721_20170523T064821_005722_00A065_C371
24	S1A_EW_GRDM_1SDH_20170523T073655_20170523T073759_016706_01BBD4_AC95
25	S1B_EW_GRDM_1SDH_20180712T063622_20180712T063722_011774_015A91_551B
26	S1B_EW_GRDM_1SDH_20180712T081506_20180712T081610_011775_015A99_069B
27	S1B_EW_GRDM_1SDH_20180712T095329_20180712T095434_011776_015AA1_622E
28	S1B_EW_GRDM_1SDH_20180712T113117_20180712T113221_011777_015AAB_68F6
29	S1B_EW_GRDM_1SDH_20180715T101734_20180715T101838_011820_015C05_73C5
30	S1B_EW_GRDM_1SDH_20180715T115554_20180715T115659_011821_015C0F_1618
31	S1B_EW_GRDM_1SDH_20180803T083127_20180803T083232_012096_01645B_91CA
32	S1B_EW_GRDM_1SDH_20180803T100924_20180803T101028_012097_016463_A4AE
33	S1B_EW_GRDM_1SDH_20180803T114744_20180803T114849_012098_01646B_4CAB
34	S1B_EW_GRDM_1SDH_20180819T062101_20180819T062201_012328_016B86_BC6C
35	S1B_EW_GRDM_1SDH_20180819T075849_20180819T075953_012329_016B8E_DB71
36	S1B_EW_GRDM_1SDH_20180828T073625_20180828T073725_012460_016FA2_3346
37	S1A_EW_GRDM_1SDH_20180828T082604_20180828T082708_023444_028D45_DE96
38	S1A_EW_GRDM_1SDH_20180906T062303_20180906T062408_023574_02915D_FE1C
39	S1B_EW_GRDM_1SDH_20180906T071139_20180906T071239_012591_0173AF_1881
40	S1B_EW_GRDM_1SDH_20190711T074226_20190711T074331_017083_020246_4FFE
41	S1B_EW_GRDM_1SDH_20190711T105837_20190711T105941_017085_020255_D6AD
42	S1B_EW_GRDM_1SDH_20190713T040923_20190713T041023_017110_02030D_04F5
43	S1B_EW_GRDM_1SDH_20190713T054725_20190713T054825_017111_020313_75B4
44	S1B_EW_GRDM_1SDH_20190713T104220_20190713T104247_017114_020328_78B9
45	S1B_EW_GRDM_1SDH_20190713T122035_20190713T122139_017115_02032E_F345
46	S1B_EW_GRDM_1SDH_20190715T084743_20190715T084847_017142_0203F5_671B
47	S1B_EW_GRDM_1SDH_20190715T102552_20190715T102656_017143_0203FD_729A
48	S1B_EW_GRDM_1SDH_20190715T120412_20190715T120517_017144_020408_6846
49	S1B_EW_GRDM_1SDH_20190722T052255_20190722T052349_017242_0206DC_96A0
50	S1B_EW_GRDM_1SDH_20190722T070127_20190722T070231_017243_0206E3_487D
51	S1B_EW_GRDM_1SDH_20190722T083944_20190722T084049_017244_0206EE_EB9D
52	S1B_EW_GRDM_1SDH_20190722T115601_20190722T115705_017246_0206FE_A276

B

Observation details

Table B.1: Observations used in scenario 1

The 37 observations used in scenario 1. "InSAR pair" is the S-1 images used for estimating ice drift and the numbers correspond to the numbers in Table A.1. The 60 sub-observations used are marked with green cells and the discarded are marked with red cells. "Time diff" is the time difference between the S-1 start-sensing-time for the second image in "InSAR pair" and the observation date. "Tot drift" is the total drift from "LAT/LON" in the "Time diff" period.

				Ice Watch classes			Classification classes				
InSAR pair	**Observation date**	**LAT**	**LON**	**PT**	**ST**	**TT**	**PT**	**ST**	**TT**	**Time diff[h]**	**Tot drift[m]**
(1, 2)	2015-02-09 07:34:00 UTC	82.4183	18.2404	6	5	nan	6	5	nan	0.86	78.6
(3, 4)	2015-02-23 13:55:00 UTC	82.8333	29.8667	5	2	nan	6	5	4	0.77	344.4
(3, 4)	2015-02-23 14:56:00 UTC	82.7833	29.6667	5	3	nan	6	5	4	0.24	13.8
(3, 4)	2015-02-23 18:15:00 UTC	82.6333	29.3000	2	nan	nan	6	5	4	3.56	40.6
(11, 12)	2015-03-15 07:52:00 UTC	82.9	20.9667	6	5	5	6	5	nan	0.83	224.9
(11, 12)	2015-03-15 09:11:00 UTC	82.9167	21.0667	6	5	5	6	5	nan	0.48	108.9
(13, 14)	2015-06-01 06:58:00 UTC	81.3256	17.2792	4.5	nan	nan	6	5	4	0.92	114.5
(15, 16)	2015-06-15 14:52:00 UTC	82.213	7.3033	4.5	nan	nan	5	4	nan	0.92	262.7
(19, 20)	2017-05-19 10:04:00 UTC	79.6983	8.0707	4.5	nan	nan	5	4	nan	2.72	47.0
(25, 26)	2018-07-12 10:02:00 UTC	85.1262	51.6167	5	nan	nan	6	5	4	1.76	12.6
(25, 26)	2018-07-12 11:03:00 UTC	85.3622	52.0357	5	nan	nan	6	5	4	2.78	188.2
(26, 27)	2018-07-12 08:35:00 UTC	84.8512	51.5925	5	nan	nan	6	5	4	1.33	79.7
(26, 27)	2018-07-12 10:02:00 UTC	85.1262	51.6167	5	nan	nan	6	5	4	0.12	5.5
(26, 27)	2018-07-12 11:03:00 UTC	85.3622	52.0357	5	nan	nan	6	5	4	1.14	13.5
(26, 27)	2018-07-12 12:30:00 UTC	85.712	52.3420	5	nan	nan	6	5	4	2.59	280.5
(27, 28)	2018-07-12 08:35:00 UTC	84.8512	51.5925	5	nan	nan	6	5	2	2.96	276.9
(27, 28)	2018-07-12 10:02:00 UTC	85.1262	51.6167	5	nan	nan	6	5	nan	1.51	462.8
(27, 28)	2018-07-12 11:03:00 UTC	85.3622	52.0357	5	nan	nan	6	5	nan	0.49	76.6
(27, 28)	2018-07-12 12:30:00 UTC	85.712	52.3420	5	nan	nan	5	4	nan	0.96	75.7
(27, 28)	2018-07-12 15:50:00 UTC	86.1078	52.1027	5	nan	nan	6	5	4	4.29	356.1
(29, 30)	2018-07-15 12:23:00 UTC	85.0867	49.9633	5	nan	nan	6	5	nan	0.43	30.8
(29, 30)	2018-07-15 13:19:00 UTC	84.8495	50.0170	6	5	nan	6	5	4	1.37	45.2
(31, 32)	2018-08-03 14:18:00 UTC	84.735	51.9800	6	5	1	6	5	nan	4.13	95.3
(32, 33)	2018-08-03 07:01:00 UTC	83.4117	52.0633	6	5	1	6	5	2	4.80	399.2
(32, 33)	2018-08-03 09:19:00 UTC	83.921	51.6933	6	5	1	6	5	4	2.50	272.4
(32, 33)	2018-08-03 10:06:00 UTC	84.0933	51.6800	6	5	1	6	5	2	1.71	276.5
(32, 33)	2018-08-03 10:48:00 UTC	84.2267	51.7683	6	5	1	6	5	2	1.01	85.0
(32, 33)	2018-08-03 14:18:00 UTC	84.735	51.9800	6	5	1	6	5	nan	2.49	86.5
(32, 33)	2018-08-03 15:03:00 UTC	84.9053	52.0188	6	5	1	6	5	2	3.24	199.7
(40, 41)	2019-07-11 05:00:00 UTC	83.6033	62.7800	5	nan	nan	6	5	4	5.99	133.3
(40, 41)	2019-07-11 08:24:00 UTC	84.2612	64.0427	4	nan	nan	5	4	nan	2.59	345.8
(40, 41)	2019-07-11 14:29:00 UTC	84.59	65.9613	6	5	nan	6	5	4	3.49	201.2
(40, 41)	2019-07-11 15:10:00 UTC	84.5217	66.0967	6	4.5	nan	5	4	nan	4.17	323.6
(44, 45)	2019-07-13 03:24:00 UTC	83.1563	59.5433	4	nan	nan	5	4	nan	8.96	235.1
(46, 47)	2019-07-15 12:50:00 UTC	82.4433	58.0167	6	4.5	nan	6	5	4	2.38	130.7
(47, 48)	2019-07-15 08:52:00 UTC	83.615	59.8300	6	4.5	nan	6	5	4	3.22	105.5
(47, 48)	2019-07-15 10:15:00 UTC	83.3028	58.5758	6	4.5	nan	6	5	4	1.84	194.0

Table B.2: Observations used in scenario 2

The 75 observations used in scenario 2. “InSAR pair” is the S-1 images used for estimating ice drift and the numbers correspond to the numbers in Table A.1. The 123 sub-observations used are marked with green cells and the discarded are marked with red cells. “Time diff” is the time difference between the S-1 start-sensing-time for the second image in “InSAR pair” and the observation date. “Tot drift” is the total drift from “LAT/LON” in the “Time diff” period. “LAT2/LON2” is the new drift corrected coordinate.

						Ice Watch classes			Classification classes				
InSAR pair	Observation date	LAT	LON	LAT2	LON2	PT	ST	TT	PT	ST	TT	Time diff[h]	Tot drift[m]
(1,2)	2015-02-09 07:34:00 UTC	82.4183	18.2404	82.4180	18.2451	6	5	nan	6	5	nan	0.86	78.6
(3, 4)	2015-02-23 07:03:00 UTC	82.6167	29.5000	82.6155	29.5366	5	1	nan	6	5	4	7.64	542.8
(3, 4)	2015-02-23 07:58:00 UTC	82.7500	29.6333	82.7422	29.8935	4	4	nan	6	5	nan	6.72	3777.7
(3, 4)	2015-02-23 09:09:00 UTC	82.8833	29.8333	82.8776	30.0078	5	1	nan	6	5	nan	5.54	2501.7
(3, 4)	2015-02-23 13:55:00 UTC	82.8333	29.8667	82.8326	29.8906	5	2	nan	6	5	4	0.77	344.4
(3, 4)	2015-02-23 14:56:00 UTC	82.7833	29.6667	82.7833	29.6677	5	3	nan	6	5	4	0.24	13.8
(3, 4)	2015-02-23 18:15:00 UTC	82.6333	29.3000	82.6332	29.3028	2	nan	nan	6	5	4	3.56	40.6
(3, 4)	2015-02-23 21:02:00 UTC	82.9000	28.0000	82.8958	28.1234	5	1	nan	6	5	4	6.34	1768.6
(3, 4)	2015-02-23 23:52:00 UTC	83.0000	27.4000	82.9913	27.6886	nan	2	nan	6	5	4	9.18	4056.7
(11, 12)	2015-03-15 07:52:00 UTC	82.9000	20.9667	82.9001	20.9830	6	5	5	6	5	nan	0.83	224.9
(11, 12)	2015-03-15 09:11:00 UTC	82.9167	21.0667	82.9167	21.0746	6	5	5	6	5	nan	0.48	108.9
(13, 14)	2015-06-01 06:58:00 UTC	81.3256	17.2792	81.3255	17.2724	4.5	nan	nan	6	5	4	0.92	114.5
(13, 14)	2015-06-01 13:55:00 UTC	81.2806	17.1301	81.2802	17.0895	4.5	3	nan	6	5	nan	6.03	690.6
(13, 14)	2015-06-01 17:25:00 UTC	81.3198	18.3182	81.3158	17.7411	4.5	nan	nan	6	5	4	9.53	9767.5
(13, 14)	2015-06-01 18:58:00 UTC	81.1800	17.1600	81.1749	16.3359	4.5	2	nan	6	5	4	11.08	14169.6
(15, 16)	2015-06-15 09:38:00 UTC	82.2083	7.4757	82.2083	7.4281	4.5	nan	nan	5	4	nan	6.16	722.3
(15, 16)	2015-06-15 13:22:00 UTC	82.2111	7.3536	82.2112	7.2382	4.5	nan	nan	5	4	nan	2.42	1750.8
(15, 16)	2015-06-15 14:52:00 UTC	82.2130	7.3033	82.2130	7.2860	4.5	nan	nan	5	4	nan	0.92	262.7
(19, 20)	2017-05-19 10:04:00 UTC	79.6983	8.0707	79.6983	8.0730	4.5	nan	nan	5	4	nan	2.72	47.0
(19, 20)	2017-05-19 11:01:00 UTC	79.8293	7.6667	79.8286	7.6942	4	nan	nan	5	4	nan	3.67	550.6
(19, 20)	2017-05-19 12:03:00 UTC	79.9750	7.2911	79.9739	7.3394	6	5	nan	5	4	nan	4.71	951.6
(19, 20)	2017-05-19 13:01:00 UTC	80.0287	7.1343	80.0270	7.2094	5	nan	nan	6	5	4	5.67	1469.8
(19, 20)	2017-05-19 14:08:00 UTC	80.0504	7.0759	80.0479	7.1844	4	nan	nan	6	5	4	6.79	2120.4
(19, 20)	2017-05-19 15:16:00 UTC	80.0690	7.0344	80.0655	7.1863	4.5	4.5	nan	6	5	4	7.92	2961.5
(19, 20)	2017-05-19 16:01:00 UTC	80.0786	6.9712	80.0742	7.1654	4	nan	nan	6	5	4	8.67	3783.0
(19, 20)	2017-05-19 17:01:00 UTC	80.1007	7.0108	80.0953	7.2483	6	4	nan	6	5	4	9.67	4618.6
(19, 20)	2017-05-19 17:56:00 UTC	80.1163	7.0839	80.1096	7.3743	4	6	nan	6	5	4	10.59	5639.3
(19, 20)	2017-05-19 19:00:00 UTC	80.1380	7.0727	80.1299	7.4234	6	4	4	6	5	2	11.66	6795.5
(25, 26)	2018-07-12 10:02:00 UTC	85.1262	51.6167	85.1262	51.6154	5	nan	nan	6	5	4	1.76	12.6
(25, 26)	2018-07-12 11:03:00 UTC	85.3622	52.0357	85.3629	52.0166	5	nan	nan	6	5	4	2.78	188.2
(25, 26)	2018-07-12 12:30:00 UTC	85.7120	52.3420	85.7064	52.3942	5	nan	nan	6	5	2	4.23	761.9
(25, 26)	2018-07-12 15:50:00 UTC	86.1078	52.1027	86.1055	52.0298	5	nan	nan	6	5	4	7.56	611.2
(25, 26)	2018-07-12 17:31:00 UTC	85.9830	50.2617	85.9698	50.2655	5	nan	nan	6	5	nan	9.25	1477.1
(26, 27)	2018-07-12 08:35:00 UTC	84.8512	51.5925	84.8506	51.5970	5	nan	nan	6	5	4	1.33	79.7
(26, 27)	2018-07-12 10:02:00 UTC	85.1262	51.6167	85.1262	51.6170	5	nan	nan	6	5	4	0.12	5.5
(26, 27)	2018-07-12 11:03:00 UTC	85.3622	52.0357	85.3621	52.0367	5	nan	nan	6	5	4	1.14	13.5
(26, 27)	2018-07-12 12:30:00 UTC	85.7120	52.3420	85.7101	52.3638	5	nan	nan	6	5	4	2.59	280.5
(26, 27)	2018-07-12 15:50:00 UTC	86.1078	52.1027	86.0988	52.1943	5	nan	nan	6	5	4	5.92	1225.4
(26, 27)	2018-07-12 17:31:00 UTC	85.9830	50.2617	85.9498	50.6230	5	nan	nan	6	5	4	7.61	4672.2
(27, 28)	2018-07-12 08:35:00 UTC	84.8512	51.5925	84.8494	51.6112	5	nan	nan	6	5	nan	2.96	276.9
(27, 28)	2018-07-12 10:02:00 UTC	85.1262	51.6167	85.1232	51.6500	5	nan	nan	6	5	2	1.51	462.8
(27, 28)	2018-07-12 11:03:00 UTC	85.3622	52.0357	85.3617	52.0414	5	nan	nan	6	5	nan	0.49	76.6
(27, 28)	2018-07-12 12:30:00 UTC	85.7120	52.3420	85.7115	52.3484	5	nan	nan	5	4	nan	0.96	75.7
(27, 28)	2018-07-12 15:50:00 UTC	86.1078	52.1027	86.1054	52.1335	5	nan	nan	6	5	4	4.29	356.1
(27, 28)	2018-07-12 17:31:00 UTC	85.9830	50.2617	85.9684	50.4528	5	nan	nan	6	5	2	5.98	2217.6
(29, 30)	2018-07-15 07:36:00 UTC	85.9818	48.6758	85.9852	48.6051	6	5	1	6	5	2	4.35	673.6
(29, 30)	2018-07-15 08:32:00 UTC	85.8048	49.9783	85.8169	49.7503	6	5	1	6	5	4	3.42	2301.3
(29, 30)	2018-07-15 11:01:00 UTC	85.4622	50.3605	85.4662	50.2983	6	5	1	6	5	4	0.93	708.2
(29, 30)	2018-07-15 12:23:00 UTC	85.0867	49.9633	85.0868	49.9604	5	nan	nan	6	5	nan	0.43	30.8
(29, 30)	2018-07-15 13:19:00 UTC	84.8495	50.0170	84.8497	50.0130	6	5	nan	6	5	4	1.37	45.2
(31, 32)	2018-08-03 14:18:00 UTC	84.7350	51.9800	84.7347	51.9887	6	5	1	6	5	2	4.13	95.3
(31, 32)	2018-08-03 15:03:00 UTC	84.9053	52.0188	84.8918	52.2157	6	5	1	6	2	nan	4.88	2469.9
(32, 33)	2018-08-03 07:01:00 UTC	83.4117	52.0633	83.4093	52.0862	6	5	1	6	5	2	4.80	399.2
(32, 33)	2018-08-03 08:14:00 UTC	83.6908	51.8467	83.6852	51.9120	6	5	1	6	5	2	3.58	1018.0
(32, 33)	2018-08-03 09:19:00 UTC	83.9210	51.6933	83.9199	51.7138	6	5	1	6	5	4	2.50	272.4
(32, 33)	2018-08-03 10:06:00 UTC	84.0933	51.6800	84.0919	51.6995	6	5	1	6	5	2	1.71	276.5
(32, 33)	2018-08-03 10:48:00 UTC	84.2267	51.7683	84.2262	51.7742	6	5	1	6	5	2	1.01	85.0
(32, 33)	2018-08-03 14:18:00 UTC	84.7350	51.9800	84.7357	51.9761	6	5	1	6	5	nan	2.49	86.5
(32, 33)	2018-08-03 15:03:00 UTC	84.9053	52.0188	84.9071	52.0156	6	5	1	6	5	2	3.24	199.7
(38, 39)	2018-09-06 10:55:00 UTC	78.8383	-5.4817	78.8394	-5.4551	nan	nan	nan	5	4	1	3.71	590.8
(38, 39)	2018-09-06 11:41:00 UTC	78.8400	-5.5000	78.8417	-5.4576	6	nan	nan	5	4	1	4.47	941.7
(38, 39)	2018-09-06 15:05:00 UTC	78.8367	-5.4883	78.8404	-5.3981	6	nan	nan	6	5	4	7.87	2000.6
(38, 39)	2018-09-06 16:55:00 UTC	78.8683	-5.0167	78.8759	-4.8201	5	nan	nan	5	4	1	9.71	4341.5
(38, 39)	2018-09-06 18:06:00 UTC	78.9100	-4.7633	78.9203	-4.4900	5	4	nan	6	5	4	10.89	6005.1
(40, 41)	2019-07-11 05:00:00 UTC	83.6033	62.7800	83.6041	62.7718	5	nan	nan	6	5	4	5.99	133.3
(40, 41)	2019-07-11 08:24:00 UTC	84.2612	64.0427	84.2632	64.0193	4	nan	nan	5	4	nan	2.59	345.8
(40, 41)	2019-07-11 14:29:00 UTC	84.5900	65.9613	84.5912	65.9473	6	5	nan	6	5	4	3.49	201.2
(40, 41)	2019-07-11 15:10:00 UTC	84.5217	66.0967	84.5237	66.0745	6	4.5	nan	5	4	nan	4.17	323.6
(44, 43)	2019-07-13 03:24:00 UTC	83.1563	59.5433	83.1544	59.5362	4	nan	nan	5	4	nan	8.96	235.1
(46, 47)	2019-07-15 12:50:00 UTC	82.4433	58.0167	82.4438	58.0088	6	4.5	nan	6	5	4	2.38	130.7
(47, 48)	2019-07-15 08:52:00 UTC	83.6150	59.8300	83.6142	59.8351	6	4.5	nan	6	5	4	3.22	105.5
(47, 48)	2019-07-15 10:15:00 UTC	83.3028	58.5758	83.3014	58.5850	6	4.5	nan	6	5	4	1.84	194.0
(49, 50)	2019-07-22 13:02:00 UTC	84.8350	59.3150	84.8448	59.2067	6	4.5	nan	6	5	4	5.99	1540.8
(51, 52)	2019-07-22 00:09:00 UTC	82.2187	52.2110	82.2259	52.1569	6	5	nan	6	5	4	11.80	1147.1
(51, 52)	2019-07-22 11:11:00 UTC	84.4308	58.9383	84.4357	58.8934	6	4.5	nan	6	5	4	0.77	732.2

Bibliography

[1] ESA sentinel online. https://sentinel.esa.int/web/sentinel/missions/sentinel-1, 2019. Accessed: 2019-10-08.

[2] The Ice Watch manual. https://icewatch.met.no/Ice_Watch_Manual_v4.1.pdf, 2019. Accessed: 2019-21-11.

[3] The Ice Watch website. https://icewatch.met.no/, 2019. Accessed: 2019-21-11.

[4] Wiebke Aldenhoff, Céline Heuzé, and Leif EB Eriksson. Comparison of ice/water classification in fram strait from c-and l-band sar imagery. *Annals of Glaciology*, 59(76pt2):112–123, 2018.

[5] M. Aulard-Macler. Sentinel-1 product definition s1-rs-mda-52-7440. Technical report, MacDonald, Dettwiler and Associates Ltd., 2011.

[6] David G Barber. Microwave remote sensing, sea ice and arctic climate. *Phys. Can*, 61:105–111, 2005.

[7] James B Campbell and Randolph H Wynne. *Introduction to remote sensing*. Guilford Press, 2011.

[8] George Casella and Roger L Berger. *Statistical Inference*. Brooks/Cole, Cengage Learning, Belmont, USA, 2th edition, 2002. ISBN 978-0-534-24312-8, 0-534-24312-6.

[9] Wolfgang Dierking. Mapping of different sea ice regimes using images from sentinel-1 and alos synthetic aperture radar. *Ieee transactions on geoscience and remote sensing*, 48(3):1045–1058, 2009.

[10] Wolfgang Dierking. Sea ice monitoring by synthetic aperture radar. *Oceanography*, 26(2):100–111, 2013.

[11] Anthony P Doulgeris and Anca Cristea. Incorporating incidence angle

variation into sar image segmentation. In *IGARSS 2018-2018 IEEE International Geoscience and Remote Sensing Symposium*, pages 8543–8546. IEEE, 2018.

[12] Charles Elachi and Jakob J Van Zyl. *Introduction to the physics and techniques of remote sensing*, volume 28. John Wiley & Sons, 2006.

[13] T Geldsetzer and J J Yackel. Sea ice type and open water discrimination using dual co-polarized c-band sar. *Canadian Journal of Remote Sensing*, 35(1):73–84, 2009. doi: 10.5589/m08-075.

[14] D. Geudtner, R. Torres, P. Snoeij, M. Davidson, and B. Rommen. Sentinel-1 system capabilities and applications. In *2014 IEEE Geoscience and Remote Sensing Symposium*, pages 1457–1460, July 2014. doi: 10.1109/IGARSS.2014.6946711.

[15] Jagvijay PS Gill and John J Yackel. Evaluation of c-band sar polarimetric parameters for discrimination of first-year sea ice types. *Canadian Journal of Remote Sensing*, 38(3):306–323, 2012.

[16] Rashpal S Gill. *SAR ice classification using fuzzy screening method*. Danish Meteorological Institute, 2002.

[17] Jörg Haarpaintner and Stian Solbø. Automatic ice-ocean discrimination in sar imagery. *Norut IT-report*, 6:28, 2007.

[18] Dan-Bee Hong and Chan-Su Yang. Automatic discrimination approach of sea ice in the arctic ocean using sentinel-1 extra wide swath dual-polarized sar data. *International journal of remote sensing*, 39(13):4469–4483, 2018.

[19] Christopher R Jackson and John R Apel. Synthetic aperture radar: marine user's manual. 2004.

[20] J. Karvonen, M. Simila, and M. Makynen. Open water detection from baltic sea ice radarsat-1 sar imagery. *IEEE Geoscience and Remote Sensing Letters*, 2(3):275–279, July 2005. ISSN 1558-0571. doi: 10.1109/LGRS.2005.847930.

[21] Juha Karvonen. Baltic sea ice concentration estimation using sentinel-1 sar and amsr2 microwave radiometer data. *IEEE Transactions on Geoscience and Remote Sensing*, 55(5):2871–2883, 2017.

[22] Anton Korosov and Pierre Rampal. A combination of feature tracking and pattern matching with optimal parametrization for sea ice drift retrieval from sar data. *Remote Sensing*, 9(3):258, 2017.

[23] Anton A Korosov and Jeong-Won Park. Very high resolution classification of sentinel-1a data using segmentation and texture analysis. In *Living Planet Symp*, page 44, 2016.

[24] Wenhui Lang, Pan Zhang, Jie Wu, Yang Shen, and Xuezhi Yang. Incidence angle correction of sar sea ice data based on locally linear mapping. *IEEE Transactions on Geoscience and Remote Sensing*, 54(6):3188–3199, 2016.

[25] Huiying Liu, Huadong Guo, and Lu Zhang. Svm-based sea ice classification using textural features and concentration from radarsat-2 dual-pol scansar data. *IEEE Journal of Selected Topics in Applied Earth Observations and Remote Sensing*, 8(4):1601–1613, 2014.

[26] Johannes Lohse, Anthony Doulgeris, and Wolfgang Dierking. Mapping of sea ice types from sentinel-1 considering surface-type dependent effect of incidence angle. *Under revision*, 2019.

[27] David G Lowe. Distinctive image features from scale-invariant keypoints. *International journal of computer vision*, 60(2):91–110, 2004.

[28] MJ Manore, DG Flett, RA De Abreu, BR Ramsay, and JJ van der Sanden. Multi-polarization sar data for operational ice monitoring. In *IGARSS 2001. Scanning the Present and Resolving the Future. Proceedings. IEEE 2001 International Geoscience and Remote Sensing Symposium (Cat. No. 01CH37217)*, volume 3, pages 1246–1248. IEEE, 2001.

[29] Iliana E Mladenova, Thomas J Jackson, Rajat Bindlish, and Scott Hensley. Incidence angle normalization of radar backscatter data. *IEEE Transactions on Geoscience and Remote Sensing*, 51(3):1791–1804, 2012.

[30] M-AN Moen, Stian Normann Anfinsen, Anthony Paul Doulgeris, AHH Renner, and Sebastian Gerland. Assessing polarimetric sar sea-ice classifications using consecutive day images. *Annals of Glaciology*, 56(69): 285–294, 2015.

[31] Stefan Muckenhuber, Anton Andreevich Korosov, and Stein Sandven. Open-source feature-tracking algorithm for sea ice drift retrieval from sentinel-1 sar imagery. *High resolution sea ice monitoring using space borne Synthetic Aperture Radar*, 2016.

[32] Robert G Onstott, Richard K Moore, and WF Weeks. Surface-based scatterometer results of arctic sea ice. *IEEE Transactions on Geoscience Electronics*, 17(3):78–85, 1979.

[33] Bruce Ramsay, Michael Manore, Laurie Weir, Katherine Wilson, and David Bradley. Use of radarsat data in the canadian ice service. *Canadian Journal of Remote Sensing*, 24(1):36–42, 1998.

[34] R. Ressel, A. Frost, and S. Lehner. A neural network-based classification for sea ice types on x-band sar images. *IEEE Journal of Selected Topics in Applied Earth Observations and Remote Sensing*, 8(7):3672–3680, July 2015.

[35] *Thermal Denoising of Products Generated by the S-1 IPF*. S-1 Mission Performance Centre, 11 2017. Reference: MPC-0392.

[36] Bernd Scheuchl, Dean Flett, Ron Caves, and Ian Cumming. Potential of radarsat-2 data for operational sea ice monitoring. *Canadian Journal of Remote Sensing*, 30(3):448–461, 2004.

[37] Suman Singha, Malin Johansson, Nick Hughes, Sine Hvidegaard, and Henriette Skourup. Arctic sea ice characterization using spaceborne fully polarimetric l-, c-and x-band sar with validation by airborne measurements. 2018.

[38] L. . Soh, C. Tsatsoulis, D. Gineris, and C. Bertoia. Arktos: an intelligent system for sar sea ice image classification. *IEEE Transactions on Geoscience and Remote Sensing*, 42(1):229–248, Jan 2004. ISSN 1558-0644. doi: 10.1109/TGRS.2003.817819.

[39] L-K Soh and Costas Tsatsoulis. Texture analysis of sar sea ice imagery using gray level co-occurrence matrices. *IEEE Transactions on geoscience and remote sensing*, 37(2):780–795, 1999.

[40] Sergios Theodoridis and Konstantinos Koutroumbas. *Pattern Recognition, Fourth Edition*. Academic Press, Inc., Orlando, FL, USA, 4th edition, 2008. ISBN 1597492728, 9781597492720.

[41] Konstantinos Topouzelis, Suman Singha, and Dimitra Kitsiou. Incidence angle normalization of wide swath sar data for oceanographic applications. *Open Geosciences*, 8(1):450–464, 2016.

[42] Costas Tsatsoulis and Ronald Kwok. *Analysis of SAR data of the polar oceans: recent advances*. Springer Science & Business Media, 2012.

[43] Natalia Zakhvatkina, Anton Korosov, Stefan Muckenhuber, Stein Sandven, and Mohamed Babiker. Operational algorithm for ice–water classification on dual-polarized radarsat-2 images. *High resolution sea ice monitoring*

using space borne Synthetic Aperture Radar, 2017.

[44] Natalia Zakhvatkina, Vladimir Smirnov, and Irina Bychkova. Satellite sar data-based sea ice classification: An overview. *Geosciences*, 9(4):152, 2019.

[45] Natalia Yu Zakhvatkina, Vitaly Yu Alexandrov, Ola M Johannessen, Stein Sandven, and Ivan Ye Frolov. Classification of sea ice types in envisat synthetic aperture radar images. *IEEE Transactions on Geoscience and Remote Sensing*, 51(5):2587–2600, 2012.